frontiers | Frontiers in Earth Science

TYPE Methods
PUBLISHED 27 August 2025
DOI 10.3389/feart.2025.1555755

OPEN ACCESS

EDITED BY
Youcun Qi,
Chinese Academy of Sciences (CAS), China

REVIEWED BY
Ricardo Reinoso-Rondinel,
KU Leuven, Belgium
Andrey Shikhov,
Perm State University, Russia

*CORRESPONDENCE
Jan Handwerker,
jan.handwerker@kit.edu

†PRESENT ADDRESSES
Gernot Geppert,
Landesamt für Digitalisierung, Breitband und Vermessung, München, Germany
Franziska Vogel,
Institute of Atmospheric Sciences and Climate (ISAC), National Research Council (CNR), Bologna, Italy

RECEIVED 05 January 2025
ACCEPTED 27 June 2025
PUBLISHED 27 August 2025

CITATION
Handwerker J, Barthlott C, Bauckholt M, Belleflamme A, Böhmländer A, Borg E, Dick G, Dietrich P, Fichtelmann B, Geppert G, Goergen K, Güntner A, Hammoudeh S, Hervo M, Hühn E, Kaniyodical Sebastian M, Keller J, Kohler M, Knippertz P, Kunz M, Landmark S, Li Y, Mohannazadeh M, Möhler O, Morsy M, Najafi H, Nallasamy ND, Oertel A, Rakovec O, Reich H, Reich M, Saathoff H, Samaniego L, Schrön M, Schütze C, Steinert T, Vogel F, Vorogushyn S, Weber U, Wieser A and Zhang H (2025) From initiation of convective storms to their impact — the Swabian MOSES 2023 campaign in southwestern Germany. *Front. Earth Sci.* 13:1555755.
doi: 10.3389/feart.2025.1555755

From initiation of convective storms to their impact — the Swabian MOSES 2023 campaign in southwestern Germany

Jan Handwerker[1]*, Christian Barthlott[1], Matteo Bauckholt[2], Alexandre Belleflamme[3], Alexander Böhmländer[4], Erik Borg[5,6], Galina Dick[7], Peter Dietrich[2,8], Bernd Fichtelmann[5], Gernot Geppert[9†], Klaus Goergen[3], Andreas Güntner[10,11], Suad Hammoudeh[3], Maxime Hervo[12], Elias Hühn[1], Milin Kaniyodical Sebastian[4], Jan Keller[9], Martin Kohler[1], Peter Knippertz[1], Michael Kunz[1], Solveig Landmark[2], Yanxia Li[4], Mehrdad Mohannazadeh[13], Ottmar Möhler[4], Mona Morsy[2], Husain Najafi[13], Nithila Devi Nallasamy[10], Annika Oertel[1], Oldrich Rakovec[13,14], Hendrik Reich[9], Marvin Reich[10], Harald Saathoff[4], Luis Samaniego[11,13], Martin Schrön[2], Claudia Schütze[2], Thorsten Steinert[9], Franziska Vogel[4†], Sergiy Vorogushyn[10], Ute Weber[13], Andreas Wieser[1] and Hengheng Zhang[4]

[1]Institute of Meteorology and Climate Research Troposphere Research (IMKTRO), Karlsruhe Institute of Technology (KIT), Karlsruhe, Germany, [2]Department Monitoring and Exploration Technologies, Helmholtz Centre for Environmental Research (UFZ), Leipzig, Germany, [3]Forschungszentrum Jülich, Institute of Bio- and Geosciences (IBG-3, Agrosphere), Jülich, Germany, [4]Institute of Meteorology and Climate Research Atmospheric Aerosol Research (IMKAAF), Karlsruhe Institute of Technology (KIT), Karlsruhe, Germany, [5]German Aerospace Center, German Remote Sensing Data Center, National Ground Segment, Neustrelitz, Germany, [6]Department Geoinformatics and Geodesy, University of Applied Sciences, Neubrandenburg, Germany, [7]Section Space Geodetic Techniques, Department of Geodesy, GFZ Helmholtz Centre for Geosciences, Potsdam, Germany, [8]Department of Geosciences, University of Tübingen, Tübingen, Germany, [9]Deutscher Wetterdienst, Offenbach, Germany, [10]Section Hydrology, Department of Geosystems, GFZ Helmholtz Centre for Geosciences, Potsdam, Germany, [11]University of Potsdam, Institute of Environmental Science and Geography, Potsdam, Germany, [12]Meteoswiss, Payerne, Switzerland, [13]Department of Computational Hydrosystems, Helmholtz Centre for Environmental Research (UFZ), Leipzig, Germany, [14]Faculty of Environmental Sciences, Czech University of Life Sciences Prague, Czechia

Since a comprehensive understanding of the water cycle cannot be developed by a single discipline alone, several institutes of the Helmholtz Association have joined forces to investigate extreme hydro-meteorological events in the framework of the 10-year "Modular Observation Solutions for Earth Systems" (MOSES) program. A key element of MOSES is conducting joint field experiments accompanied by coordinated modeling activities. A recent example is the "Swabian MOSES" campaign in southwestern Germany in 2021 involving several university institutes and the German Weather Service (DWD). In the summer of 2023, a second campaign, "Swabian MOSES 2023" was conducted that extended and complemented the first one in several ways. The study area was enlarged to stretch from Mount Feldberg in the southern Black Forest to

around Tübingen in the Neckar Valley. The former is known for the frequent initiation of thunderstorms, which then intensify and propagate northeastward, causing a hotspot for hail and heavy precipitation in the Neckar Valley. The "trigger area" around Feldberg was equipped with radars, Doppler wind lidars, radiosondes, a microwave radiometer, energy balance stations, meteorological towers, hail sensors, Global Navigation Satellite System (GNSS) stations, and optical disdrometers. The downstream "impact area", in particular in the Lindach Valley, a small catchment near Tübingen, was equipped with two energy balance stations, a cosmic ray neutron sensing (CNRS) sensor, a gravimeter, hail sensors, and optical disdrometers for detailed studies of the hydrological impacts. A mobile CRNS device carried out measuring tours through the impact area, and a mobile storm-chasing team launched swarmsondes into several thunderstorms. These observational data are used to validate meteorological (ICON, ICOsahedral Non-hydrostatic) and hydrological (mHM, ParFlow) models. This paper describes the concept of the observation campaign and the accompanying modeling activities and shows some illustrative first results. In the future, we plan to assimilate the campaign observations into the high-resolution numerical model ICON to (i) bridge gaps between observations and (ii) assess the impact of additional observations on the model analysis and forecasts using targeted data denial experiments.

KEYWORDS

field campaign, convective storms, hydrometeorological extremes, soil moisture, aerosols, ground-based remote sensing, precipitation, ICON model

1 Introduction

High-impact hydro-meteorological events usually involve a chain of processes and interactions between natural and human-made factors. Therefore, they remain challenging to be monitored, understood, and predicted in their full complexity with current observational networks and numerical weather prediction (NWP) models (Merz B. et al., 2020; Weber et al., 2022). Several institutes of the Helmholtz Association in Germany recently joined forces to investigate relevant event chains from evolution to impacts using a coordinated observational and modeling concept. This cooperation is known as MOSES (Modular Observation Solutions for Earth Systems; Weber et al., 2022). Part of this initiative focuses on severe convective events that cause hail, heavy rain, flash flooding, and a deterioration of water quality. The concept includes storm initiation, intensification, and decay as well as ensuing impacts such as runoff generation, flooding, input of pollutants into streams, and hail and storm damages across disciplines and scales. This approach was first tested in 2019 in the framework of a campaign in the Ore Mountains on the Czech-German border (Wieser et al., 2022). Amongst other things, interfaces for data exchange and communication channels were defined in this context. In the summer of 2021, the first full-blown observational campaign was carried out in the Neckar Valley between Rottenburg and Tübingen under the name of "Swabian MOSES 2021" (Kunz et al., 2022). The region is known to be a local thunderstorm and hail hotspot (Puskeiler et al., 2016), and in fact, several severe convective storms were observed in detail during the campaign. However, it turned out that the often long-lasting storms developed far upwind of the study area. This motivated a second campaign in the summer of 2023 with a study area that was significantly extended upstream of the prevailing southwesterly flow. We therefore deployed our instruments in a region where thunderstorms were expected to initiate (the "trigger area") and in a region where the effects of the thunderstorms could be observed (the "impact area").

Despite recent improvements in numerical weather prediction (NWP), e.g., by higher grid resolution, improved parameterizations of physical processes, ensemble modeling strategies, or post-processing techniques, accurate forecasts of convective precipitation and hail, not to mention their impacts, are still a challenge. Cloud formation and subsequent precipitation generation result from a chain of complex dynamical and microphysical processes and often create large forecast uncertainty. The development of deep convection requires a sufficient amount of moisture in the lower troposphere, convective instability, and a trigger mechanism such as diurnal thermal heating, orographic forcing, or lifting by convergence zones or lines, which are often limited to widths of a few kilometers (e.g., Wilson and Schreiber, 1986). Although the ingredients for triggering convection are largely known, forecast skill remains generally low (e.g., Barthlott and Hoose, 2015). A large part of the uncertainty results from the models' difficulties in initiating convective processes at the right place and time. As the grid resolution of operational NWP models is on the order of 2–4 km, orographic or turbulent triggers remain (at least partly) unresolved. For example, the adequate simulation of a supercell storm from the Swabian MOSES 2021 field campaign required a grid spacing of 1 km or less (Barthlott et al., 2024). Generally, the representation of the dynamic and thermodynamic structure of the lower troposphere is particularly challenging in complex terrain (Rotach et al., 2022), and more observations than usually available are required to sufficiently constrain the initial conditions for NWP during data assimilation. Although convection-permitting ensemble prediction systems account for

uncertainties in initial (and also lateral boundary) conditions and in the representation of physical processes, the predictions are often underdispersive, motivating further research to effectively represent all relevant sources of uncertainty (e.g., Barthlott et al., 2022). For deep convective clouds, this includes in particular nonlinear microphysical effects and the competing pathways in a complex microphysical system (e.g., Seifert et al., 2012; Schneider et al., 2019), as well as local environmental conditions such as soil moisture. A better understanding of convection initiation, cloud formation, precipitation, and their impact on and interaction with hydrology is essential for evaluating and possibly improving the NWP chain.

In the process chain of hydro-meteorological extreme events, triggered by convective storms, the primary hydrological impact is (flash) flooding. In the case of high-relief terrains, such as the Swabian MOSES 2021 "impact area", the topography is complex and river corridors and valleys are narrow, requiring precipitation and stream stage-discharge information to be extremely local (Merz R. et al., 2020). In this context, hydrological models may be further expanded by hydrodynamic flood inundation modeling (Najafi et al., 2024). Integrated hydrological models that treat surface and subsurface hydrodynamics in a continuum approach, with 3D subsurface hydrodynamics, which account for mass and energy transfers with the atmosphere, can resolve km-scale heterogeneity, hill slope processes, and, e.g., streamflow aquifer interactions (Brookfield et al., 2023). These strong soil moisture-precipitation feedbacks (Koster et al., 2004; Dirmeyer et al., 2009) influence the land-water balance and soil moisture distribution. These effects are associated not only with extreme short-term precipitation events but also with increased soil moisture and groundwater levels along river valley convergence zones, driven by water redistribution across the landscape. This redistribution modifies land-atmosphere coupling and, through scale-dependent feedbacks, impacts the hydro-meteorology of coupled atmospheric models (Barlage et al., 2021). However, such type of groundwater-soil moisture coupled climate models are not yet utilized in the current Swabian MOSES campaign.

Improving hydrological models crucially depends on additional observations. For example, the assimilation of earth observations such as terrestrial water storage anomaly (GRACE) and land surface temperature (LSA-SAF) has contributed to improve the partitioning of subsurface fluxes (Rakovec et al., 2016a) and to reduce the predictive uncertainty of the estimated evapotranspiration (ET) (Zink et al., 2018). Moreover, it has been shown that observed streamflow time series, which are commonly used to calibrate hydrological models, are a necessary but not sufficient condition to ensure a proper distribution of the incoming precipitation into spatially distributed water storage components such as soil moisture and evapotranspiration (Rakovec et al., 2016b). For these reasons, mobile a cosmic ray neutron sensing (CNRS) combined with latent heat observed with *in-situ* eddy covariance stations could help to improve the parametrization of hydrological models.

Given the remaining uncertainties in monitoring and predicting high-impact hydro-meteorological extreme events, Swabian MOSES 2023 is designed to build scientific and methodological bridges between the trigger and the impact areas of our study domain, between hydrology and meteorology, and between measurements and modeling through interdisciplinary and cross-institutional cooperation. It is inspired to some extent by recent campaigns and modeling studies on convection in other parts of the world (e.g., Nesbitt et al., 2021; Varble et al., 2021). The underlying hypothesis of Swabian MOSES 2023 is that the effects observed in the impact area can be traced back to the developments in the trigger area. We use reliable information on soil moisture to better constrain the surface energy balance and the overall state of the lower atmosphere, while information on precipitation and irradiation is, in turn, needed to interpret changes in soil moisture better and derive hydrological impacts as part of the process-based event chain. Hydrological models are run using meteorological observations and different atmospheric models as input data and produce detailed spatio-temporal soil moisture information, which in turn may feed back into the atmosphere, as well as flood inundation information for selected catchments. For atmospheric modeling, we run high-resolution, multi-member ensembles with advanced microphysics. Observations from the campaign will be assimilated into meteorological and hydrological models to gauge their impact on the forecasts, to fill observation gaps in a physically consistent manner, and to verify simulations. This general approach is part not only of the campaign presented here but of the entire MOSES program.

As an extension to the Swabian Moses 2021 measurement campaign, we first expanded the measurement area and divided it into trigger and impact areas. Additional operational measurements from lidars and radars from MeteoSwiss and Meteo France were integrated. In addition, some new measuring devices (DIAL and Raman lidar) were used at least on a test basis, and some citizens participated in the sense of "citizen science", e.g., by reporting large hailstones. The use of our measurements for assimilation into the ICON model in cooperation with the German Weather Service represents an important step towards the close integration of measurement and model. It not only enables investigations into the impact of individual measurements on the model result, but also allows the analysis to be used as an extension of atmospheric observation in space and time.

This manuscript describes the concept of Swabian MOSES 2023 and therefore lays a foundation for future, more detailed investigations. As this project is a follow-up of the activities in 2021, we will frequently refer to the overview paper about the predecessor campaign by Kunz et al. (2022). Section 2 provides an overview of the Swabian MOSES 2023 measurement campaign. It is followed by a section on the experimental setup and one on the numerical modeling activities. Some first results and highlights are shown in Section 5 before conclusions and a short outlook are given in Section 6.

2 Overview about the Swabian MOSES 2023 activities

During the measurements in 2011, (Kunz et al., 2022) several significant thunderstorm events were observed. However, the origin of the thunderstorms was to the southwest and thus outside the area equipped with measuring devices at that time. Therefore in 2023, we installed most of the meteorological measurements in the region around Mount Feldberg, southwest of the investigation area of Swabian MOSES 2021 (*cf.* Figure 1). As we assumed that this is where many thunderstorms initiate that later affect the central Neckar valley between Tübingen and Göppingen, we called this region the "trigger area". Accordingly, we refer to the latter as the "impact area". Disdrometers and hail sensors, energy balance stations, and soil moisture measurements were concentrated in this

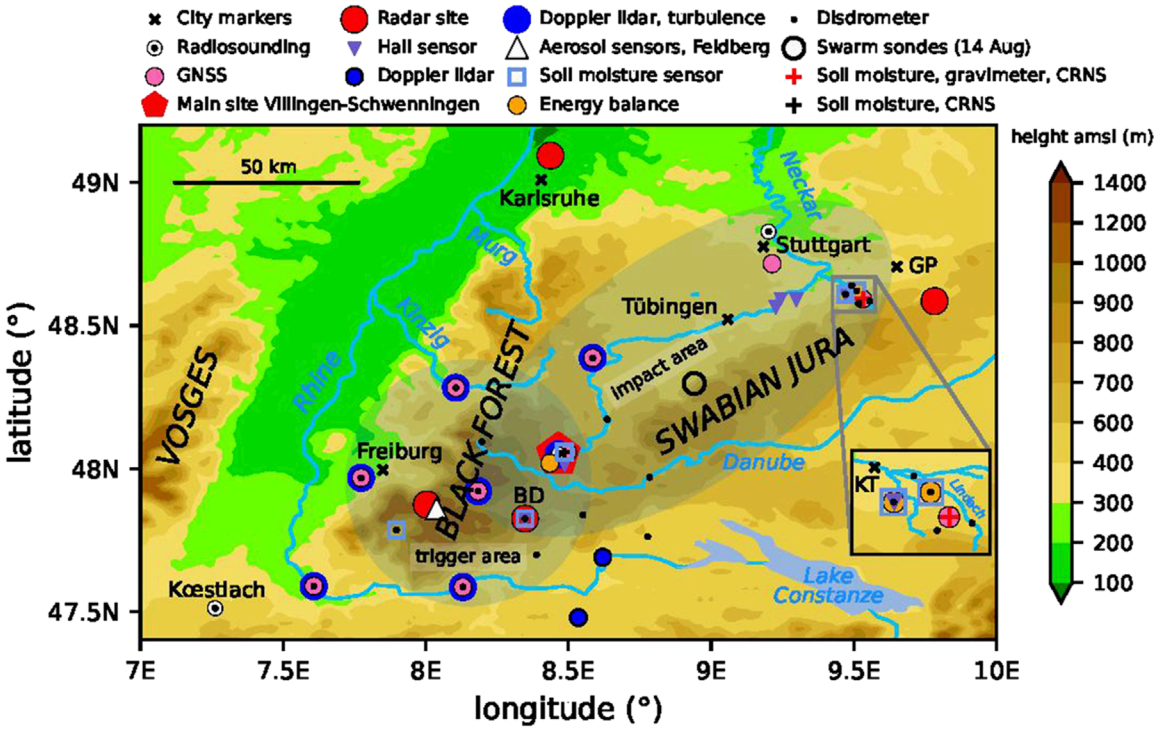

FIGURE 1
Overview of the study area, which is embedded in the Black Forest and Swabian Jura mountain ranges, between which the Neckar flows from Villingen-Schwenningen (main site) to Kirchheim unter Teck (KT) and then on to Stuttgart. The "trigger area" is located around Mount Feldberg, including the cities of Freiburg and Villingen-Schwenningen, whereas the "impact area" is found between the cities of Tübingen and Göppingen (GP). The focus there is on the catchment of the Lindach river. The X-band radar is sited in Bonndorf (BD).

region. It was demanding to identify a suitable catchment area for all the planned hydrological investigations. The decision to focus on the Lindach River was influenced by several factors: its size, location, the presence of operational river gauging stations, and the significant impact of karst on the Swabian Jura region.

The joint measurement phase was carried out over 2 months in June and July 2023 with multiple measuring devices continuously monitored and maintained. Unless unfavorable weather was foreseeable for several days, daily weather briefings were held in the morning to decide over which periods measurements should be intensified. A decision matrix was used, which was developed as part of MOSES (*cf.* Wieser et al., 2022). During the eight intensive observation phases (IOP), additional radiosondes were launched in Kœstlach and at the KITcube main site. The latter was manned around the clock by two people during IOPs. After the main measurement phase, most devices remained in operation but were no longer maintained, and there were no weather briefings, radiosonde ascents, or personnel on site. However, several thunderstorms occurred in August, which were sufficiently well recorded for us to include them in our investigations.

The measurement data were collected in near real-time at a central location during the measurement campaign and were made available to all participating partners. For this purpose, all sensors except the radiosondes were connected to the Internet. Radiosonde data were provided manually as soon as the measurement was completed. Moreover, a data transfer to the German Weather Service (DWD) was set up for near real-time data assimilation, which, however, could not be realized as planned and was, in the end, performed after the campaign. We hope to use the resulting analysis data to fill gaps, i.e., to obtain reliable information about the state of the atmosphere at unobserved locations. Independent of our measurements, model runs with the ICON (ICOsahedral Non-hydrostatic) model (Zängl et al., 2015) at different spatial resolutions and with different microphysics schemes were performed, using our measurements for validation purposes. Finally, hydrological modeling is carried out for the entire study area, yielding detailed soil moisture information. We can focus on this because the Lindach catchment is highly instrumented.

3 Experimental setup

At the KITcube main site[1] in Villingen-Schwenningen radiosondes were released during IOPs in a rhythm of 3 h. If necessary, the time sequence could be condensed to 90 min. The IOP-related measurements were supplemented by continuous measurements: A microwave radiometer enabled the continuous determination of temperature and humidity profiles, as well as the liquid water content and integrated water vapor (IWV). An

1 Please find a tabular overview of all instruments in the suplementary file.

energy balance station made it possible to observe the near-surface development of standard meteorological variables (temperature, air humidity, air pressure, precipitation, wind direction, wind speed, and precipitation), the components of the radiation budget as well as the energy budget over a field of growing sunflowers. In addition to the surface temperature, profiles of the soil temperature and soil moisture were also measured down to a depth of 50 cm (5 cm, 10 cm, 20 cm, 50 cm). Data was recorded with a temporal resolution of 10 min. Turbulent fluxes were calculated based on 30 min using the software packages EddyPro-7.0.9 SOl and TK3.1 (Mauder et al., 2013).

An autolauncher was located near Kœstlach in the area of the Burgundian Gate (Burgundische Pforte) in France to obtain the state of the atmosphere upstream during IOPs. The radiosondes were launched at a time interval of 6 h.

The investigation area is covered by the operational C-Band precipitation radars of DWD located in Türkheim (at the eastern end of the Swabian Jura), Feldberg (southern Black Forest), and Memmingen. The northern part of the area is covered by C-Band radar at KIT Campus North, north of Karlsruhe. To perform dual Doppler studies with the Feldberg radar, our X-Band (Kalthoff et al., 2013) radar was sited in Bonndorf, about 26 km east from Feldberg. Unfortunately, there was a technical problem with this radar, so measurements will only be available here from July 11th. The locations of all radars but Memmingen are indicated in Figure 1. Radar Memmingen is located about 85 km southeast from the impact area. All radars operated in simultaneous dual-pol mode with a volume repetition time of 5 minutes. The DWD radars and our X-Band radar performed a 10 elevation scan with elevations from 0.5° up to 24°. The C-Band radar in KIT Campus North performs 14 Elevations from 0.4° to 30°. Measuring ranges and radial resolutions are 180 km/250 m for DWD radars, 120 km/500 m for KIT Campus North, and for the X-Band in Bonndorf 100 km/500 m.

As ground truth reference for KIT C- and X-Band radar data regarding precipitation intensity, but also to the size distribution of hydrometeors, a network of 24 optical disdrometers was quite evenly distributed, mainly within the range of our X-band radar in Bonndorf. Five of them were located in the impact area.

There were six so-called mesostations, each equipped with a Doppler Wind Lidar, providing a continuous measurement of the wind profile, an optical disdrometer, a GNSS receiver, a cloud camera, and a meteorological tower to measure the standard near-surface meteorological variables. These are air temperature, humidity, air pressure, wind speed, wind direction, and precipitation. Data was aggregated to 10 min means.

To characterize the aerosol in air masses potentially being included in convective systems downwind of the Black Forest, we conducted comprehensive aerosol measurements (*cf.* Figure 2) on the summit of Mt. Feldberg from 15 June to 26 July 2023. This location is next to a DWD station equipped with various meteorological instruments, including a cloud radar. We measured the spatial distribution, ice nucleation activity, number concentration, size distribution, and chemical composition of aerosol particles, as well as concentrations of various trace gases potentially serving as precursors of secondary aerosol particles. We used a scanning aerosol lidar to measure vertical and horizontal aerosol distributions, cloud levels, and boundary layer heights (Zhang et al., 2022). The scanning lidar did zenith scanning measurements from elevation angles of 90° to 0° with steps of 5° in two directions and with a temporal resolution of around 15 (30) min during the IOPs (EOP). A Portable 1ce Nucleation Experiment (PINE; Möhler et al., 2021) was used to perform *in situ* measurements of the concentrations of ice nucleating aerosol particles. PINE measured the ice nucleation activity of the aerosol particles at a temperature of 252 K with a temporal resolution of 6 min. In addition, filter samples were collected every second day and analyzed in the laboratory for ice nucleating particle numbers using the Ice Nucleation Spectrometer of the Karlsruhe Institute of Technology (INSEKT; Schneider et al., 2021). The filter-based analysis provides a higher sensitivity for INP concentrations. In addition to the data shown here for 252 K, it covers the range from 268 to 248 K. The chemical composition of the aerosol particles was determined online with a high-resolution aerosol mass spectrometer (NH_4^+, SO_4^{2-}, NO_3^-, Organics, for $PM_{2.5}$) and a CHARON PTR-MS (semi-volatile organics and NO_3^-, for $PM_{1.0}$). Black carbon was measured with an aethalometer. The PTR-MS was also used to measure the less oxidized volatile organic compounds (VOC). Different trace gas monitors were used to determine the concentrations of O_3, NO_2, and CO_2. A compact meteorology sensor was used to observe wind speed, direction, humidity, temperature, radiation, and precipitation. Particle number concentrations were counted with two different CPC, particle size distributions were measured with a scanning mobility sizer, an optical particle counter, and an aerodynamic particle sizer in the overall range between 10 nm and 18 μm. All instruments were mounted on two containers of 16′ and 8’. The aerosol sampling was done via stainless steel tubes with a TSP (total suspended particles) and a $PM_{2.5}$ inlet located on the roof of the container about 3.7 m above ground level. Trace gases were sampled via Teflon (FEP) tubes at the same location.

Following the near-surface measurements during Swabian MOSES 2021, time series of soil moisture and temperature were measured *in situ* at six sites at three depths with two sensors each at 5-min intervals using time-domain transmission soil moisture sensors and temperature sensors with custom-made data logger systems (Kunz et al., 2022). The specific observation depths were determined during installation at each site based on local soil profiles. Readings were transferred to the database every 12 h to provide near real-time monitoring. Three soil moisture stations were installed throughout the trigger area and three within the impact area to obtain data from the entire study area.

Cosmic ray neutron sensing (CRNS) sensor, is an innovative technique used to measure soil moisture and snow water equivalent over large areas (Zreda et al., 2012). The advantage of CRNS over traditional point-based sensors is its ability to cover a large footprint of typically 10–20 ha (Köhli et al., 2015), making it ideal for monitoring hydrological processes at the field to landscape scales. In the present study, a sensor was deployed in a stationary position to provide continuous, non-invasive measurements at the KITcube site near Villingen-Schwenningen. In addition, mobile CRNS campaigns further extended the utility of this method by mapping the spatial distribution of soil moisture and snowpack in the whole region. Mounted on vehicles, mobile neutron detectors can cover extensive terrains, sensing average water content at a distance of up to 200 m from the road and revealing its spatial variation due to factors like topography, vegetation, and land use (Schrön et al., 2018). By providing high-resolution data on water distribution, mobile CRNS

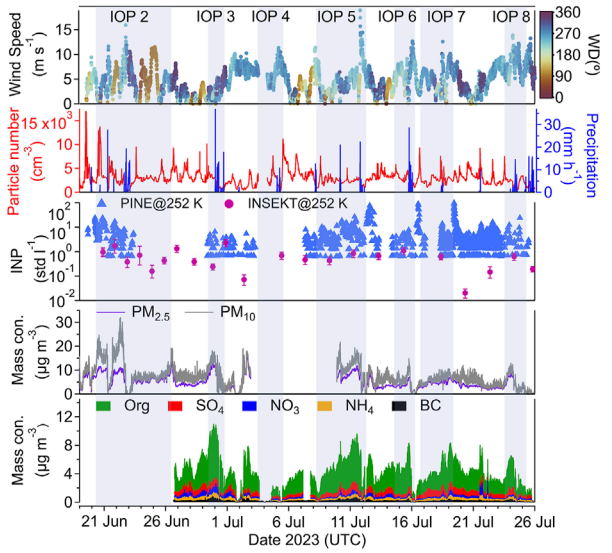

FIGURE 2
Overview of aerosol parameters observed on the summit of the Feldberg for a period covering six IOPs. The upper panel shows wind speed and direction, the second panel shows aerosol particle number and precipitation, the third panel gives the number of ice nucleating particles (INP) per standard liter for a temperature of 252 K from an on-line method (PINE) and filter samples (INSEKT), the fourth panel shows the evolution of particulate mass for particles smaller than 2.5 and 10 µm, and the lowermost panel shows the aerosol particle composition: organics, sulfate, nitrate, ammonium, chloride, and black carbon for $PM_{2.5}$.

measurements have the potential to improve our understanding of hydrological dynamics and support better decision-making in water resource management and extreme weather events. In the present study, several mobile CRNS campaigns have been conducted with a car across the Lindach catchment and beyond before and after prospective rain events to obtain information on soil moisture along transects towards regional scales.

In addition, water storage variations including larger soil depths were monitored with terrestrial gravimetry. By monitoring the temporal variations of the Earth's gravity acceleration, gravimeters are sensitive to mass variations due to water storage changes in the surroundings of the instrument. In this campaign, we continuously operated a gPhone relative gravimeter located in the impact area in an energy-self-sufficient container, the Solar Cube, as described in Wieser et al. (2022).

Automatic hail sensors were operated at six locations across the impact area (see Figure 1). The sensors detect each hailstone hitting a sensing area of approximately 0.2 m^2 and convert the resulting signal into hail kinetic energy and diameter. None of the sensors were affected by hail during the entire field campaign.

In addition to the *in-situ* measurements, soil moisture values were derived from remote sensing data as time series for the location of the soil moisture network and as maps for the whole area for specific days. We initially employed the Soil Moisture Active and Passive Mission (SMAP) satellite, utilizing its most recent (version 5) Level 4 SM data assimilation product. By integrating measurements from radar and radiometers, it delivers surface and root-zone soil moisture with a spatiotemporal coverage of 2–3 days and 9 km × 9 km. The Advanced Microwave Scanning Radiometer 2 (AMSR2) instrument aboard GCOM-W is the second type. We implement it to detect the moisture content of the surface soil using passive microwave sensors. The spatial-temporal coverage of the system is 10 km × 10 km and 1 day. The most recently implemented data type is SMOS (Soil Moisture and Ocean Salinity Mission). Monitoring soil moisture levels on a global scale is a sophisticated and specialized undertaking. It provides worldwide coverage with a spatial resolution of 35–50 km in less than 3 days. To ensure a high degree of precision and certainty, the gauge measurements will be compared to the three mission measurements.

Satellite-based remote sensing is the realistic way to estimate evapotranspiration (e.g., Richter, 1996; 2003; Wloczyk, 2007). To model radiation components such as long-wave surface radiation and net radiation, remotely sensed geo-bio-physical variables such as albedo, emissivity, and the Normalized Difference Vegetation Index (NDVI) are employed. Based on these variables, components of the energy balance can be modeled, including the convective heat flux and the latent heat flux. The knowledge of these parameters enables the derivation of real evapotranspiration for the Landsat overflight time. The satellite-based determination of evapotranspiration is based on the analysis of Landsat data from the spectral bands red, near and short-wave infrared, and thermal band (8–12 µm). The data is evaluated concerning its cloud- or haze-free surface visibility. The following figures illustrate results for the NDVI and the real evapotranspiration of a part of the Swabian MOSES region. The entire test area is covered by scenes 26 and 27 of paths 194 and 195.

At GFZ, the Global Navigation Satellite System (GNSS) raw data from stations of global and regional ground networks are operationally analyzed in near-real time. The Zenith Path Delay (ZPD) and IWV measurements are used to improve weather forecasts and are also utilized in various scientific investigations. Currently, more than 500 stations are in operational evaluation, including about 300 stations of the German SAPOS network, the stations of the European EUREF network, and global IGS stations. As a part of the observing system, the GFZ installed eight additional GNSS stations in the region of interest and operated them in near-real time during the measurement campaign (Figure 1).

Two energy balance stations were operated in the northern part of the impact area. The main goal was to record evaporation as a component of the water balance. The measurements were taken in Dettingen unter Teck on a 4 m high mast and in Weilheim an der Teck on an 8 m high mast. Both measurements were taken over grassland. Turbulent fluxes were calculated based on 30 min.

A mobile storm chasing team was equipped with a drone to take aerial images of hailstones, an automated hail sensor to observe hail spectra, and Sparv windsondes/swarmsondes to measure *in situ* vertical profiles of temperature, humidity, and wind in the updraft of severe thunderstorms. The latter allows for estimating pseudo-Lagrangian trajectories (Markowski et al., 2018), which are crucial for the maximum size of hailstones. The system with small (yogurt cup size) and light (12 g) sondes allows the user to launch a swarm of sondes nearby. The team was in operation for 13 days across the entire investigation area and launched a total of 26 swarmsondes (no hail measurements on the ground). The public was also informed about our experiment via radio. They were asked to report any hail observations to us.

TABLE 1 Model configuration for the ICON simulations.

Model aspect	Setting
Initial and boundary data	6.5 km ICON-EU analyses, 3 h update
Initialisation time	00:00 UTC
Integration time	24 h
CCN activation from aerosol particles	using pre-calculated activation ratios stored in look-up tables (Segal and Khain, 2006)
Heterogeneous ice nucleation	based on mineral dust concentrations (Hande et al., 2015)
Homogeneous ice nucleation	following Kärcher and Lohmann, (2002) and Kärcher et al. (2006)
Land-surface model	multi-layer land-surface scheme TERRA (Heise et al., 2006)
Turbulence parameterization	1D based on prognostic equation for the turbulent kinetic energy (Raschendorfer, 2001)
Radiation scheme	ecRAD (Hogan and Bozzo, 2018), called every 12 min

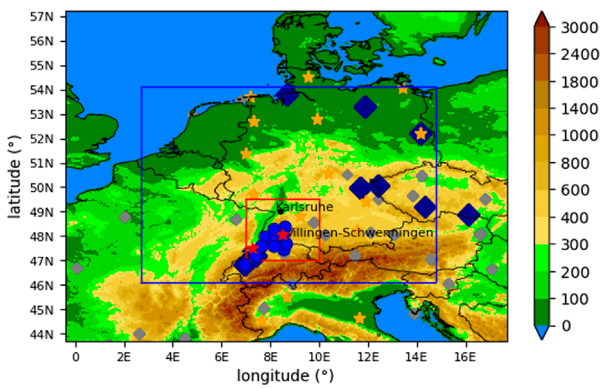

FIGURE 3
ICON 2 km simulation domain and model orography in meters above sea level. The blue rectangle depicts the 1 km simulation domain and the red one the MOSES domain depicted in Figure 1. The colored markers show the operational radiosounding and wind profiler network with observations that are actively assimilated in the operational forecast suite at DWD, exemplary for 02 June, 11:00 UTC. Operational radiosoundings (orange markers) and operational wind profiler sites are actively assimilated (dark blue markers). The dense SWM 2023 measurement network is also shown, including SWM radiosounding sites in Villingen-Schwenningen and Kœstlach (red markers), and Doppler wind lidar sites (blue markers). The grey markers show operational wind profiler sites that are excluded from the assimilation.

TABLE 2 Campaign observations intended to be used for meteorological data assimilation in the ICON/KENDA system. Shown are, respectively, variables, the measurement system, and the type of observation used for assimilation in the ICON/KENDA system.

Variable	Instrument	Observation Type
T2m, RH2m, Ps	met. mast	SYNOP
T2m, RH2m	energy balance	SYNOP
Vertical profiles of u,v	Doppler wind lidar	PILOT
T, RH, u, v	targeted radiosondes	TEMP
Z (radar reflectivity)	X-band radar	EMVORADO
v_D (Doppler velocity)		
ZPD (zenith path delay)	ground-based GPS receiver	GPSGB
SPD (slant path delay)		

4 Numerical modeling and data assimilation

4.1 Atmospheric modeling

The Swabian MOSES field campaign provides an exceptional data set of atmospheric and hydrological measurements that need to be combined with numerical modeling. Thus, we perform hindcasts of individual IOP days to study the impact of the orography, soil moisture, and various microphysical uncertainties on the predictability of deep convection. These simulations can help to interpret observational results and depict potential model deficiencies.

Numerical results of a supercell storm from the Swabian MOSES 2021 field campaign showed that only an ICON configuration with a double-moment scheme assuming the right Cloud Condensation Nuclei (CCN) concentration combined with a finer grid spacing (i.e. 1 km) can adequately simulate this event (Barthlott et al., 2024). This study showed the benefits of using an aerosol-aware double-moment microphysics scheme for convective-scale predictability and that the use of different CCN concentrations can determine whether a supercell is successfully simulated or not.

We use the ICON model, which is also used operationally by the DWD, in two configurations with different horizontal and vertical grid spacing: (i) the 2 km R19B07 grid, which

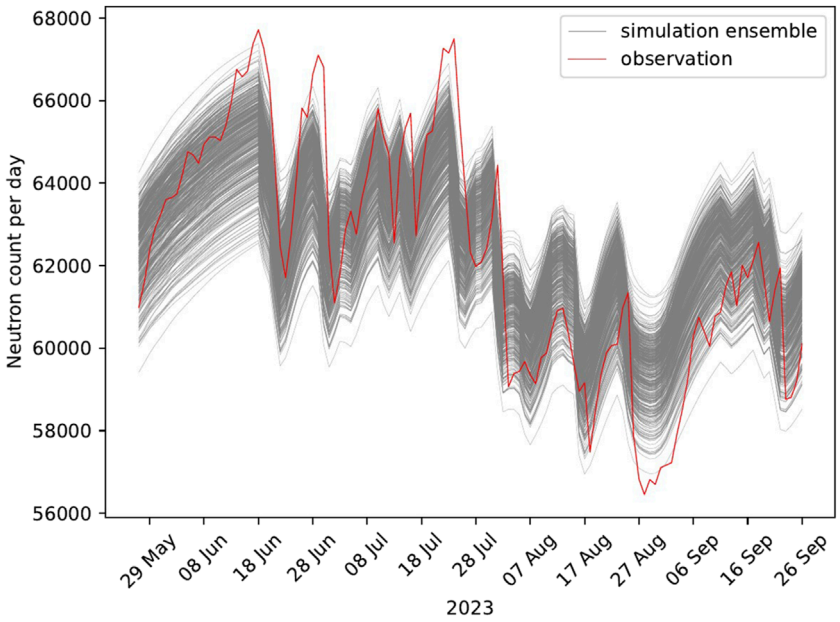

FIGURE 4
Analyzing Neutron Counts: A comparison of observed data from the 2023 MOSES Campaign at Villingen-Schwenningen site with estimated CRNS Neutron Counts by mHM, covering the period from 23 May 2023 to 27 September 2023. The mHM simulations are derived from the Neckar catchment configuration, utilizing 500 parameter sets to generate 500 realizations.

corresponds to the operational ICON-D2 configuration at DWD, and (ii) a 1 km R19B08 grid embedded in the former. The height-based, terrain-following vertical coordinates are based on the vertically stretched Smooth Level Vertical (SLEVE) coordinate implementation (Leuenberger et al., 2010). The number of vertical levels is 65 at 2 km and 100 at 1 km horizontal grid spacing. Deep convection is explicitly represented at 2 km grid spacing and only shallow convection is parameterized using the Tiedtke-Bechtold scheme (Bechtold et al., 2008; Tiedtke, 1989). The latter is omitted at 1 km grid spacing. We use a time step of 20 s for 2 km, and 10 s for a horizontal grid spacing of 1 km. In 2023, DWD used a single-moment (1MOM) microphysical scheme for operational weather forecasting. Cloud condensation nuclei (CCN) activation is not explicitly simulated, and the condensed mass is determined by saturation adjustment (see, e.g., Barthlott et al., 2017). We also use this scheme as a reference but perform further simulations with the double-moment microphysics scheme (2MOM) by Seifert and Beheng, (2006) to simulate aerosol effects. Further model settings are given in Table 1. The microphysical uncertainties addressed here comprise the scaling of cloud condensation nuclei (CCN), ice nucleating particles (INP), the width of the cloud droplet size distribution, and the sedimentation velocity of graupel. The simulation domain for both resolutions is given in Figure 3.

Besides model evaluation, the Swabian MOSES 2023 data are also used to determine the uncertainty ranges of the perturbed parameters. E.g., concentrations of ice nucleating particles (INPs) throughout the operation time were used to determine the range of scaling of the INP concentration in the ICON model.

4.2 Meteorological assimilation and validation

To validate the representation of flow patterns in the NWP system, which, for example, can play a major role in convection initiation (see Section 1), additional observations are beneficial. Although the operational observation network includes a relatively large number of sites, it cannot sufficiently observe the mesoscale characteristics across complex terrain, for example, due to insufficient observation coverage (Figure 3).

The observation network from the SWM 2023 campaign provides the opportunity for a detailed comparison of the flow represented in the operational regional analysis dataset (ICON-D2) to observations. In particular, the dense network of Doppler wind lidars provides unique observations available for validation (and assimilation) of vertical profiles of the horizontal wind (Figure 1). These observations of vertical profiles of the horizontal wind are routinely retrieved from wind profilers or radiosondes, which have poor spatial and spatiotemporal coverage, respectively (Figure 3). The ICON-D2 analysis is available hourly on the 2 km grid (Reinert et al., 2024).

To further exploit the full potential of the extended network of campaign observations, suitable observations will be assimilated in the quasi-operational assimilation and forecasting system of DWD to provide a high-resolution campaign re-analysis dataset covering the campaign period. This dataset will provide the best possible coherent 4D description of atmospheric conditions, taking into account the campaign observations and could be used as initial and/or boundary data for numerical modeling and sensitivity experiments (see Section 4.1). We aim to make this dataset accessible

TABLE 3 List of performed IOPs and further events observed after the end of the official measuring phase.Times are indicated in UTC. The daily maximum radar-derived rain amount max R in the Swabian MOSES domain in mm, the number of targeted radiosoundings (RS) in Villingen-Schwenningen and Kœstlach (VS/KOE) during each IOP,as well as CRNS rover measurements are shown. BF, SJ, VOS, and RV depict the Black Forest, Swabian Jura, Vosges mountains, and Rhine valley.

No	Date	Comment (maximum radar-derived 24-h precipitation amount)	RS	Rover
1	07 June 05:00	few isolated cells over BF (12.8)	14/4	yes
	08 June 23:00	widespread isolated cells with heavy precipitation mainly focused over mountainous area (69.6)		-
2	20 June 05:00	cells initiated over southern BF in the afternoon, large translation speed towards northeast (33.3)	26/14	-
	21 June	larger convective cells move into the domain from the southwest in the morning and move over southern BF and SJ, no convection in the afternoon (52.5)		-
	22 June	weak showers in the afternoon over the BF and RV, long-lived convection in northern Germany with heavy precipitation and potential supercells (93.4)		-
	23 June 05:00	no precipitation		yes
3	29 June 17:00	convective cells from southwest intensify over southern VOS mountains before midnight (27.9)	11/5	-
	30 June 23:00	nocturnal convection over the BF dissipating until 11:00 UTC, localized single cells in the afternoon with low precipitation amounts in entire domain (90.8)		yes
4	03 July 17:15	convective cells develop over southern BF and northern VOS area in late evening (19.8)	12/8	-
	04 July	weakening showers in morning hours, convective rain over VOS mountains in the afternoon and evening, no rain in the BF area, initiation of a potential supercell after 21:00 UTC west of Lake Constanze (28.5)		-
	05 July 14:00	passage of frontal rain in the morning, no rain in the afternoon (38.3)		-
5	08 July 05:00	decaying showers in southern parts of VOS and BF in the morning, rest of the day rain-free (36.2)	38/25	-
	09 July	single cells with weak rain intensities over the southern BF, northern part of VOS, and RV in the afternoon (19.4)		-
	10 July	convective cells come in from the west and travel towards the east in the early morning hours, no rain afterward (31.4)		yes
	11 July	strong convective cells develop in late afternoon moving eastwards, entire MOSES domain covered with rain (73.5)		yes
	12 July 05:00	some weak showers decaying in the early morning, potential supercell initiation in the afternoon outside of observational domain (89.1)		-
6	14 July 17:00	no precipitation	11/6	-
	15 July	squall-line structured precipitation passes in the evening from southwest (58.0)		-
	16 July 05:00	cells move out of the domain until 06:00 UTC (34.8)		-
7	17 July 20:00	no precipitation	9/6	-
	18 July	weak cells traveling from west to east around noon and in the afternoon, in the evening with large translation speeds in the northern part of the domain (47.4)		-
	19 July 05:00	convective cell initiated over VOS mountains in the early morning passing the entire MOSES area towards the east (13.2)		-
8	23 July 17:00	decaying showers in northern part of the domain (7.0)	10/6	
	24 July	convection moves in from France in the morning with orographic enhancement over the BF, frontal precipitation in the afternoon (55.1)		yes
	25 July 05:00	more stratiform rain in northeastern part of the domain (35.3)		
A	04 August	many thunderstorms, hail in Reutlingen (65.0)		-
B	14 August	intense thunderstorm formed leeward of BF and moved northeast (46.3)		yes
C	24 August	many thunderstorms crossed the BF, potential supercell northeast of Villingen-Schwenningen (62.2)		-

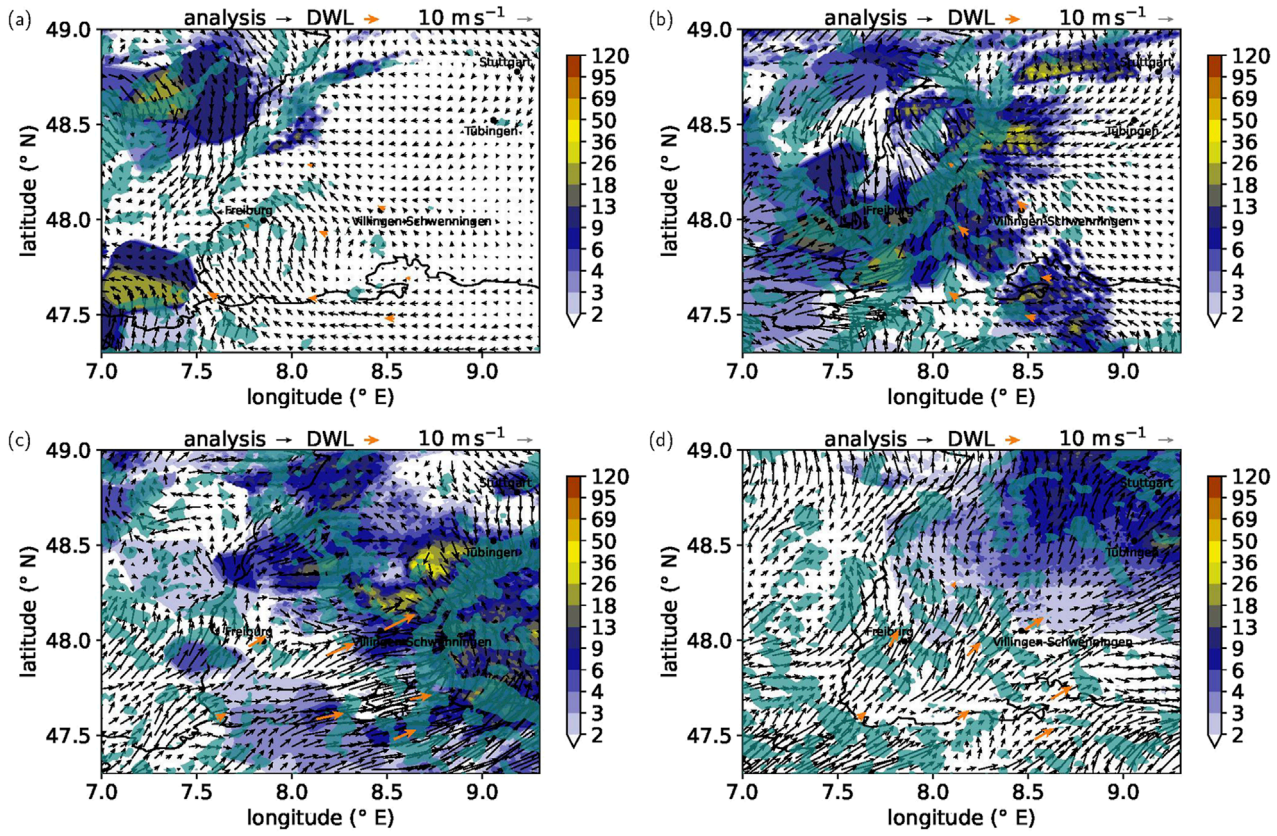

FIGURE 5
ICON-D2 analysis wind field 500 m agl (black arrows) and wind convergence larger than $3.5 \cdot 10^{-4}$ s^{-1} (turquoise shades) on 11 July from 18:00 UTC **(a)** to 21:00 UTC **(d)** with 60-min RADOLAN precipitation rate (in mm h^{-1}, colors). Precipitation is accumulated approximately from the time shown in **(a–d)** plus 1 h. The orange arrows show the observed wind field at Doppler wind lidar sites.

to be used in future analyses of the campaign. Furthermore, the re-analysis dataset can be used for re-forecast experiments to quantify forecast improvement through the availability of additional observations during forecast initialization.

For data assimilation, the ICON model will be employed in a convection-permitting configuration. The regional ensemble forecasting system is coupled to the convective-scale data assimilation system KENDA (Schraff et al., 2016), which is based on a Local Ensemble Transform Kalman Filter (LETKF; Bishop et al., 2001; Hunt et al., 2007). A relatively large number of campaign observations will be assimilated in designated experiments, such as surface temperature, humidity, and pressure, vertical profiles of the horizontal wind components, and targeted radiosondes (Table 2). These observations will supplement the operational observations.

4.3 Hydrological and flood impact modeling

The main goal of the hydrological modeling is twofold. The first objective is to evaluate the skill of the mesoscale hydrological model mHM (Samaniego et al., 2010; Kumar et al., 2013) and the integrated hydrological model ParFlow (including the Common Land Model (CLM) model) (Kuffour et al., 2020; Belleflamme et al., 2023) in reproducing state variables such as soil moisture (SM) anomalies.

The modeling setup of mHM is based on the latest 1 km version of the German Drought monitor, which was recently evaluated against a set of diverse types of soil moisture and streamflow observations (Boeing et al., 2022; 2024). In this stage, the parameters of mHM are estimated via inverse modeling using daily streamflow records. The procedure will follow the protocol proposed by Rakovec et al. (2016b).

For mHM, the second objective is to determine whether the model's skill or its maneuverability across domains or resolutions increases when observations obtained during the MOSES campaign are included in the data estimation procedure. Figure 4 shows simulations of mHM using Desilets equation (Desilets et al., 2010; Fatima et al., 2023) after calibration with neutron count observation at Villingen-Schwenningen from May to September 2023 to reproduce the neutron counts observations derived from the CRNS sensor. Each ensemble, in Figure 4, represents a mHM run based on a specific parameter set that is obtained by calibrating mHM using a Dynamically Dimensioned Search (DDS) algorithm and a random seed. A comparison between the 500 ensemble members and the observed CRNS at Villingen-Schwenningen shows a minimum, maximum, and mean Kling–Gupta efficiency (KGE, Gupta and Kling, 2011) of 0.47, 0.62, and 0.54, respectively. With the default

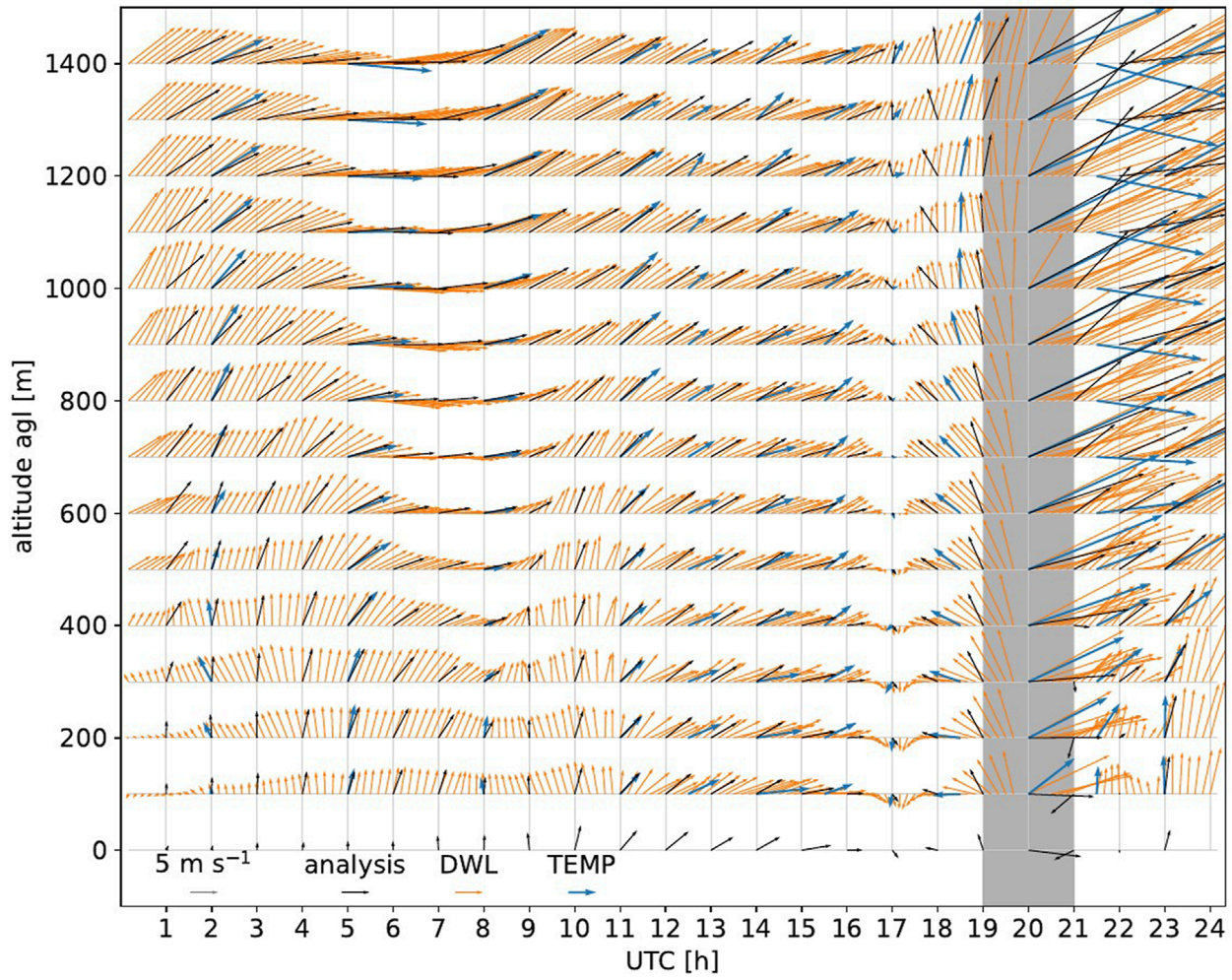

FIGURE 6
Evolution of vertical profiles of wind direction and speed above ground level (arrows) on 11 July at KITcube main site in Villingen-Schwenningen. Shown are 10 min Doppler wind lidar observations (DWL; orange), 1 h ICON-D2 analysis (black), and radiosonde measurements launched in Villingen-Schwenningen (TEMP; blue). The precipitating period from 19 to 21 UTC is highlighted in grey.

setting of mHM (i.e., without calibration), the model performance yields KGE of 0.53. Hence, the best parameter set with KGE 0.62 is used for simulations and forecasting of soil moisture.

The underlying soil properties of mHM simulation are based on the BÜK200 (BGR, 2014) with three prescribed soil layers of the following depths: 50 mm, 250 mm, and 600 mm. For calibration of mHM, daily meteorological forcings were used. The precipitation data was taken from HYRAS (Rauthe et al., 2013), the average temperature was interpolated by External Drift Kriging (EDK) (Samaniego et al., 2011), and potential evapotranspiration was estimated by Hargreaves-Samani method (Hargreaves and Samani, 1985). In the evaluation phase, the same daily forcing was used, although mHM disaggregates the outputs of the model to an hourly temporal resolution, allowing for more detailed insights into short-term soil moisture variability and forecast accuracy.

We extend the mHM chain consisting of the atmospheric and hydrological models by deploying the hydrodynamic flood inundation model RIM2D (Apel et al., 2022) in selected catchments of the Swabian area. Hence, we implement a model chain to simulate and forecast severe flood impacts. In the current approach, we go beyond the recent work by Najafi et al. (2024) and explore the capabilities of flood impact forecasting for comparably small-scale convective storms and resulting flash floods. For this, we drive the model chain by the novel experimental SINFONY ("Seamless INtegrated FOrecastiNg sYstem", Blahak, 2025) data from the DWD that merge nowcasting and numerical weather prediction in a consistent product. The hydrodynamic model RIM2D is a raster-based flood inundation model based on the inertia formulation of the shallow water equations (Bates et al., 2010). Driven by water discharge simulations from the mHM hydrological model, it continuously simulates water depth, flow velocities and inundation extent along river reaches. Further flood impact indicators, such as human and vehicle stability in flood water, affected buildings, roads, and critical infrastructure elements, can be derived from the simulation results and maps of exposed assets. The RIM2D model is an exemplary setup for the lower reaches of the Fils and Murr catchments. These catchments were, however, not affected by any IOP events in 2023. Nevertheless, the available data and

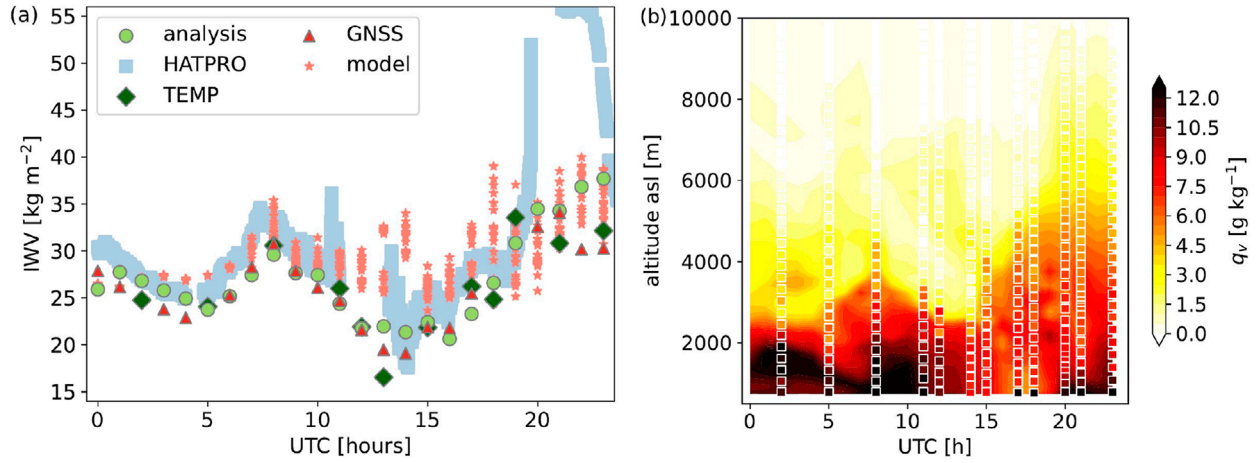

FIGURE 7
Evolution of specific humidity on 11 July 2023 (IOP5) at KITcube main site. **(a)** Evolution of IWV (kg m^{-2}) retrieved from radiosondes (TEMP, diamond), microwave radiometer (HATPRO; square), GNSS (triangle), and ICON-D2 analysis (circle) data as well as from a microphysical model ensemble (model, asterisk) with differing horizontal resolution and CCN activation (Section 4.1). Microwave radiometer measurements were removed when the rain flag was raised. **(b)** Evolution of vertical profiles of specific humidity (q_v, in g kg^{-1}) from the ICON-D2 analysis (shading) and specific humidity measurements from radiosondes (colored squares). For visualization, only every 50th measurement of the radiosondes is shown.

models allow for establishing and testing an innovative flood impact forecasting model chain, which creates a simulation infrastructure for future campaigns in the years to come.

The modeling setup of ParFlow/CLM is described in further detail in Belleflamme et al. (2023), including an evaluation against observational data (*in-situ* and remote sensed data from satellites) for soil moisture, evapotranspiration, groundwater table depth, and river discharge. In this setup, the integrated hydrological model ParFlow (Kuffour et al., 2020) and its internal land surface module CLM have been deployed at 0.6 km resolution over Germany and the neighboring regions in the framework of a quasi-operational monitoring and forecasting system for subsurface water resources. As atmospheric forcing, we use the first 24 h of each daily HRES run, the high-resolution deterministic forecast from ECMWF (European Centre for Medium-Range Weather Forecasts). ParFlow/CLM is run at an hourly resolution with hourly forcing, and outputs are stored every 3 hours. This setup has already been used successfully in the context of extreme weather events by comparing the impact on river discharge of several radar-based precipitation products for the 2021 flood event in the Eifel mid-mountain range (western Germany) (Saadi et al., 2023).

5 First results and highlights

5.1 Summary of IOPs during Swabian MOSES

In the first 2 months of the campaign, eight IOPs were conducted (Table 3). In August, three particularly interesting events numbered A–C occurred with thunderstorms in the Black Forest region. The IOPs comprised in total of 25 days during which about 200 targeted radiosondes were launched and seven CRNS rover measurements were conducted. As a rough estimate of the rain amount that occured during each IOP, the maximum radar-derived rain amount in the Swabian MOES domain is given in that table in mm. Sections 5.2 and 5.3 highlight ongoing modeling activities and first measurement results for IOP 5 and Event B (14 August 2023) to illustrate the potential and challenges of the Swabian MOSES 2023 campaign observations.

5.2 IOP5

IOP5 started on 8 July 2024 at 05:00 UTC and lasted until 12 July 05:00 UTC. On the first day, convection developed in the southwestern part of the MOSES domain only. Weak showers were initiated on 9 and 10 July, but the main event occurred on 11 July, as indicated by Radar Online Adjustment (RADOLAN; Bartels, 2004) observations (Figures 5, 8e). The RADOLAN data set combines weather radar data with hourly surface precipitation observations of about 1,300 automated rain gauges all over Germany to get quality-controlled, high-resolution (1 km) quantitative precipitation estimations. Towards the evening, precipitation developed west of the Black Forest region and passed across the Black Forest and the Swabian Jura (Figure 5). The precipitating region is accompanied by an elongated low-level convergence zone. During the passage of the main precipitation north of the KITcube main site, the low-level wind direction at the KITcube main site turned rapidly from south-easterly flow to south-westerly flow (Figures 5, 6). The upper-level flow remained southwesterly during the day. The overall low-level flow pattern represented by the ICON-D2 analysis agrees with the measurements by the Doppler wind lidar network (Figures 5, 6). Yet, local differences prevail (Figure 6). For example, at the KITcube main site, wind direction differences between ICON-D2 analysis and Doppler wind lidar observations of several degrees are present (Figure 6). The errors are particularly large in the evening

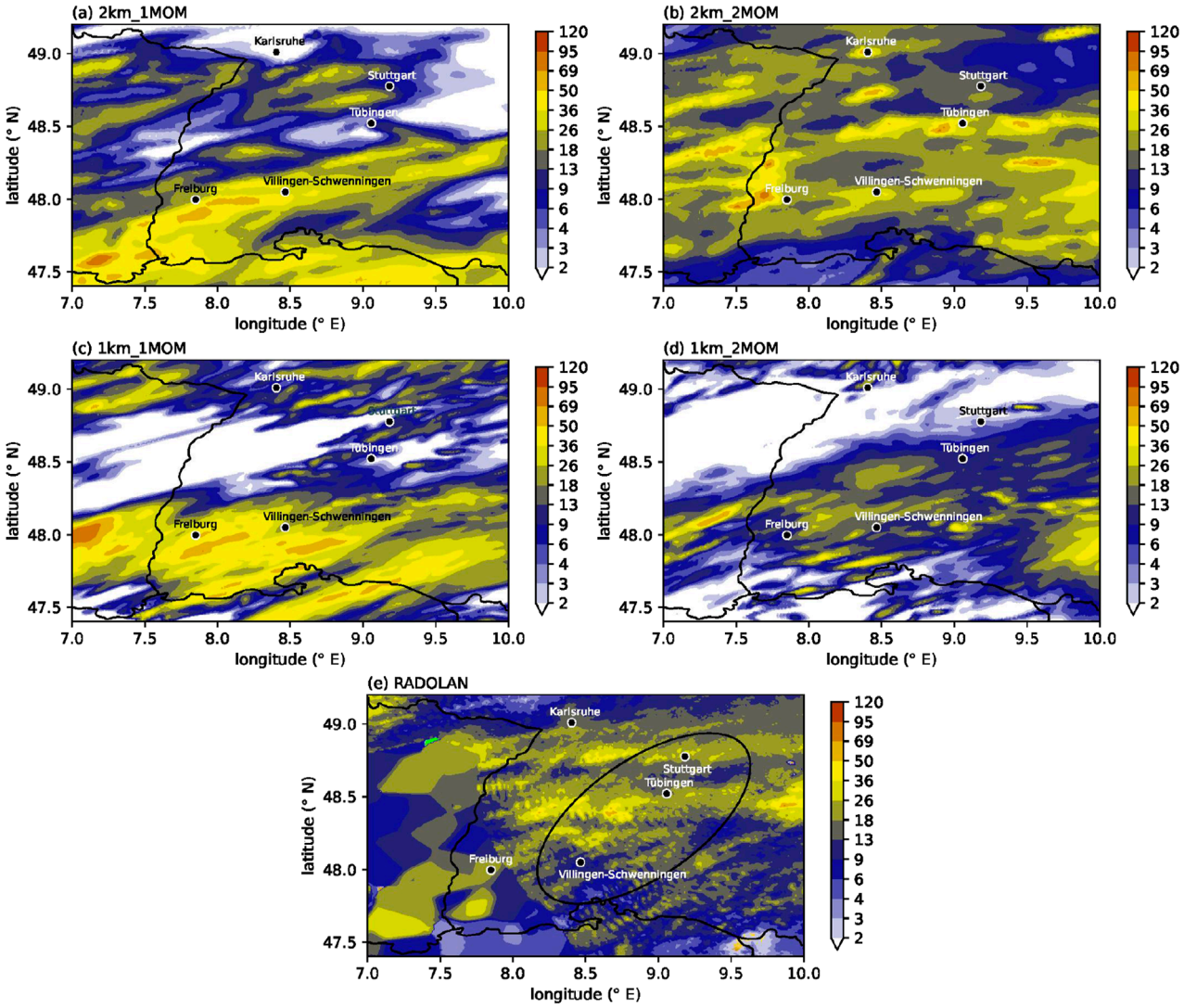

FIGURE 8
Simulated 24 h precipitation amounts in mm for 11 July with 2 km and 1 km horizontal grid spacing and single- and double-moment microphysics scheme **(a–d)**; Radar-derived 24 h precipitation amount in mm from RADOLAN **(e)**. The coarser resolution in the southwestern part of the domain is due to an outage of the Feldberg radar at that time, and the black ellipsis represents the impact area already depicted in Figure 1.

when the precipitation passes north of the main site. This indicates that the ICON-D2 analysis can represent the overall flow pattern relatively well, while local differences from the observations are present. While overall good agreement between the profiles of the horizontal wind retrieved from radiosondes and the Doppler wind lidar is present throughout the morning and early afternoon, both measurements do not fully agree during the passage of the precipitation event and afterward. If and how these mesoscale flow patterns influence the forecasts of the precipitation event could be analyzed in data impact experiments in the future. Strong convection developed on 12 July as well, but in the western part of the domain, and therefore too far away from most instruments in the field.

Several hours before the precipitation event on the evening of 11 July, observations and model data show a gradual moistening of the atmosphere (Figure 7a). While absolute values of integrated water vapor content (IWV) vary between measurement systems and ICON-D2 analysis and simulations, they agree w.r.t. the overall temporal evolution of IWV. IWV estimated from radiosondes as well as from GNSS measurements match fairly well, and IWV retrieved from the microwave radiometer tends to slightly overestimate IWV values at the KITcube site in Villingen-Schwenningen, in particular during the precipitation event. The substantial overestimation of IWV by the microwave radiometer due to the wetting of the sensor illustrates the need for careful observation post-processing, e.g., for model validation and potential future assimilation purposes. The ICON simulations with different grid spacing and microphysics parameterizations show a remarkable spread in IWV after only several hours of lead time and also match the observations fairly well (Figure 7a).

The frequent radiosonde launches during IOP 5 show the evolution of the vertical profile of specific humidity and

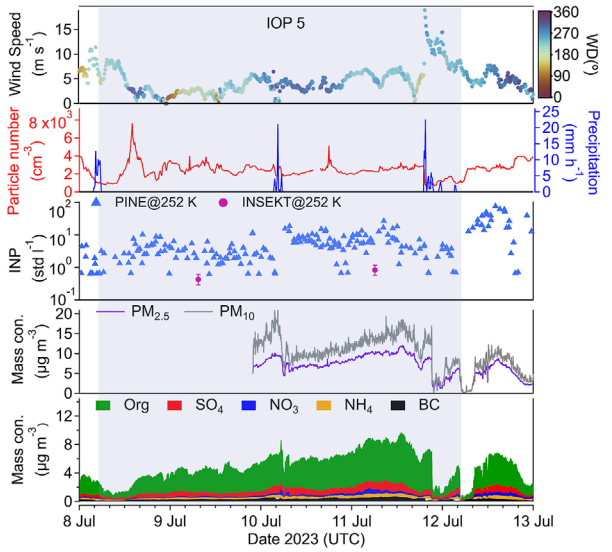

FIGURE 9
Overview of aerosol parameters observed on the summit of the Feldberg during IOP5. The upper panel shows wind speed and direction, the second panel shows aerosol particle number and precipitation, the third panel gives the number of ice nucleating particles (INP) per standard liter for a temperature of 252 K from an online method (PINE) and filter samples (INSEKT), the fourth panel shows the evolution of particulate mass for particles smaller than 2.5 and 10 µm, and the lowermost panel shows the aerosol particle composition: organics, sulfate, nitrate, ammonium, chloride, and black carbon.

illustrate substantial moistening of the troposphere up to 6 km altitude in the second half of 11 July (Figure 7b). The overall specific humidity structure is well represented in the ICON-D2 analysis compared to the radiosonde observations. However, local differences of up to ±2 K arise, for example, because local vertical humidity gradients are shifted vertically by several meters (Figure 7b).

The ICON simulations initialized at 00:00 UTC with operational analysis data show substantially different precipitation patterns depending on the setup (Figure 8). The ICON model operating with operational settings (i.e. 2 km horizontal grid spacing and single-moment microphysics scheme) simulates a large precipitation area in the southwestern part of the MOSES domain oriented towards the North-East (Figure 8a). This overestimation compared to observations is reduced when a more sophisticated double-moment scheme is used (Figure 8b). The location of the main precipitation area to the South of Tübingen is in much better agreement with the RADOLAN observations. In addition, the strong precipitation at the Swiss border simulated with the single-moment scheme is also reduced. Interestingly, the runs with 1 km grid resolution show a worsening of the results (Figures 8c,d), indicating that higher grid resolution is not always beneficial. Possible reasons could be that with 1-km grid spacing, the model still operates in the grey zone where some processes start to be resolved, but are still parameterized (e.g., shallow convection). However, the improvement of the results using the double-moment at 2 km grid spacing points towards the benefits of using a more advanced microphysics scheme for operational NWP.

The role of different CCN concentrations for cloud formation based on observations in the trigger area (see Section 5.2.1) will be investigated with the ICON model in the future. Moreover, simulations with the model system ICON-ART (Aerosol and Reactive Trace gases) are planned to enable the treatment of atmospheric chemistry and aerosols (Rieger et al., 2015). In an accompanying study, INP concentrations in the model are adjusted within the range of observed variability to investigate the influence of microphysical uncertainties on the forecasting of deep moist convection.

5.2.1 Aerosols in the trigger area during IOP5

IOP5 was characterized by an overall increase in particle mass from about 4 to 8 µg m^{-3} of non-refractory components with the organics dominating (Figure 9). The total aerosol particle number concentrations were relatively stable with values around 3,000 cm^{-3}. Also, the number of ice nucleating particles remained relatively stable between 1–10 per liter during IOP5. The wind speeds ranged between 1–10 m s^{-1} with gusts up to 20 m s^{-1} on the evening of July 11 with westerly directions but the local temperatures were among the highest during the campaign with an average of about 293 K. These high temperatures most likely contributed to higher VOC emissions by the black forest trees and substantial secondary organic aerosol formation. The particle size distributions indicate dust particles near the mountain top during the middle and the end of IOP5 with 2–5 µg m^{-3} of particle mass of particles larger than 2.5 µm. However, this was significantly less than during IOP2 with 10–15 µg m^{-3} of particles larger than 2.5 µm. Each significant precipitation event was associated with a strong decrease in aerosol particle mass, indicating washout. From the fingerprint information of the high-resolution mass spectra, aerosol particle sources will be determined and compared with the results of the ICON-ART model.

5.2.2 Spatial soil moisture distributions

During the IOP periods, seven CRNS Rover measurements have been carried out to study the spatial soil moisture distribution in the impact area. Among other days, 11 July 2023 is particularly interesting due to the relatively dry conditions. The measurements were carried out between 07:20 UTC and 14:02 UTC. During that period, no precipitation was measured in this area, nor was any precipitation simulated. The measurement area of the CRNS was naturally limited to accessible roads, while the footprint area around the detector spans diameters of up to 400 m and measurement depths of up to 30 cm. The measurement route passed several distributed stationary soil moisture sensors in the Lindach catchment. The absolute value of soil moisture derived from the CRNS rover has been calibrated on these anchor points.

As the simulated soil moisture fields do not vary with time, we compare the observed soil moisture to simulations valid between 10:30 and 12:00 UTC depending on the availability of the model output. ICON analyses and ICON forecasts (initialized at 00:00 UTC of the same day) with double-moment microphysics show similar volumetric water contents of around 25%–30% for most of the domain with decreasing values towards the North (Figures 10a,b). Compared to the measurements, the ICON model is mostly too moist, and the observed high spatial

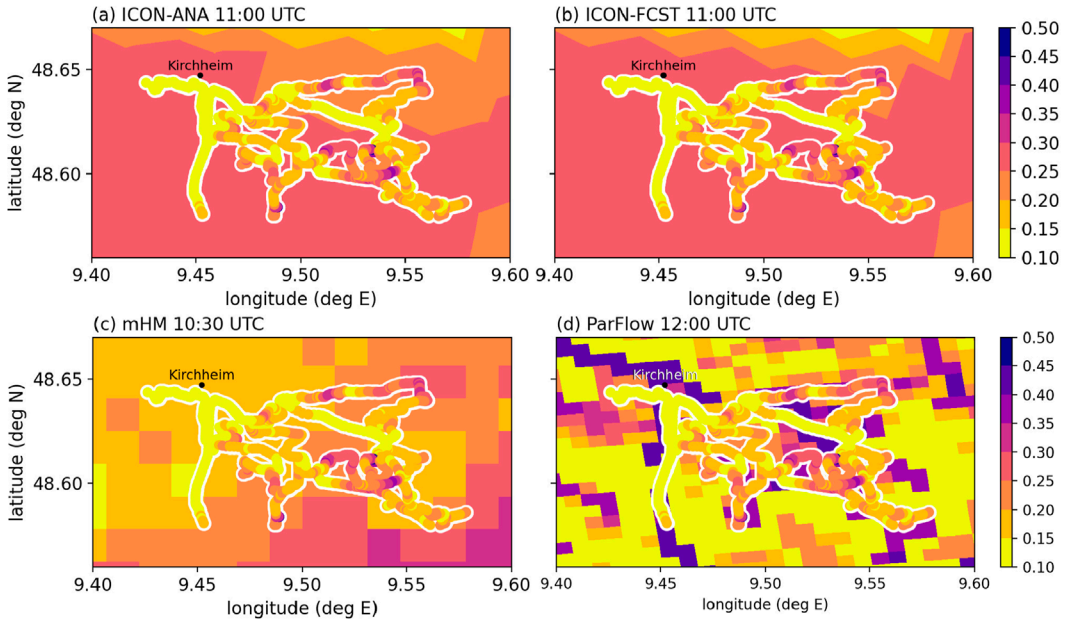

FIGURE 10
Volumetric water content in m^3 m^{-3} from ICON analyses **(a)**, ICON forecasts with double-moment microphysics **(b)** until a depth of 27 cm below the surface, from mHM simulations **(c)** until 30 cm, and from ParFlow simulations **(d)** until 30 cm, overlaid with CRNS Rover observations valid for a depth of approximately 25 cm.

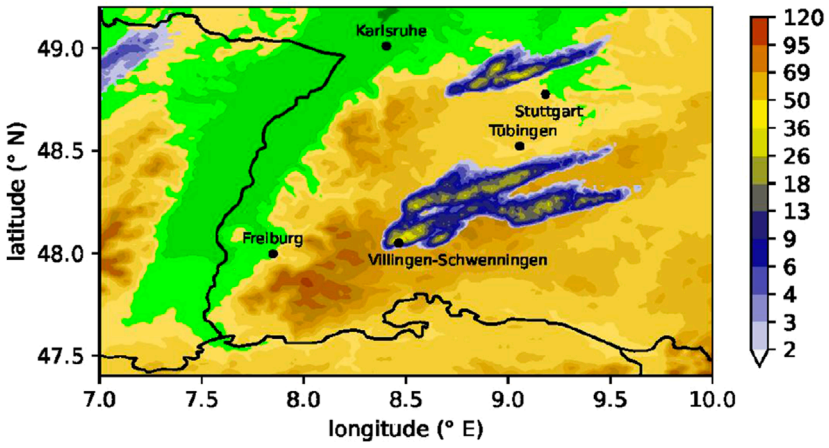

FIGURE 11
Radar-derived precipitation amount from RADOLAN on 14 August between 06:00 and 24:00 UTC.

variability is not captured. This has important implications for the evolution of the boundary layer, as soil moisture controls the partitioning of the available energy at the ground into sensible and latent heat.

A better representation of soil moisture is apparent from the mHM soil moisture simulations as shown in Figure 10c. The mHM model more accurately captures the spatial pattern of soil moisture as observed indirectly by the Rover. Based on the results in Figure 10c, future studies could make use of the measured neutrons or their soil moisture product to further improve hydrological model states and forecasts.

The volumetric soil water content simulated by ParFlow/CLM also yields results similar to those obtained from the CRNS rover (Figure 10d). In particular, it captures the low values in the western part of the catchment. Due to its high spatial resolution, it also presents a high spatial heterogeneity similar to that of the CRNS rover. ParFlow, with its free-surface overland flow boundary condition, simulates surface and subsurface flow in a continuum approach. Contrary to mHM and ICON, ParFlow simulates the lateral subsurface water flow, leading to convergence areas along the river valleys. The grid cell width of 0.6 km is much larger than the Lindach river width, which explains the (too) high volumetric water

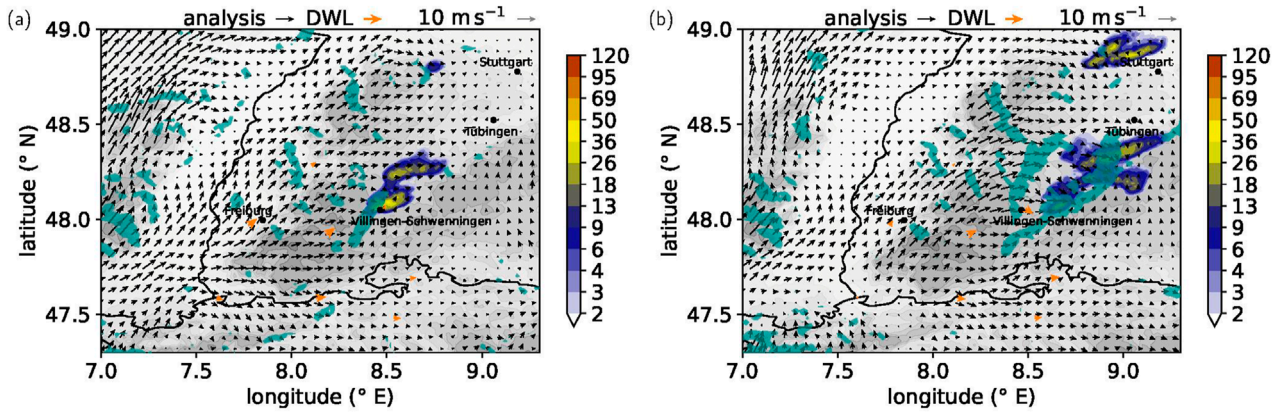

FIGURE 12
ICON-D2 analysis wind field 500 m agl (black arrows) and wind convergence larger than $3.5{\cdot}10^{-4}$ s^{-1} (turquoise shades) on 14 August at 11:00 UTC **(a)** and 12:00 UTC **(b)** with 60-min RADOLAN precipitation rate (in mm h^{-1}, colors) accumulated from 10:50 UTC to 11:50 UTC **(a)** and 11:50 UTC to 12:50 UTC **(b)** (*cf.* Figure 14). The orange arrows show the observed wind field at Doppler wind lidar sites (DWL). Grey shading outlines the topography.

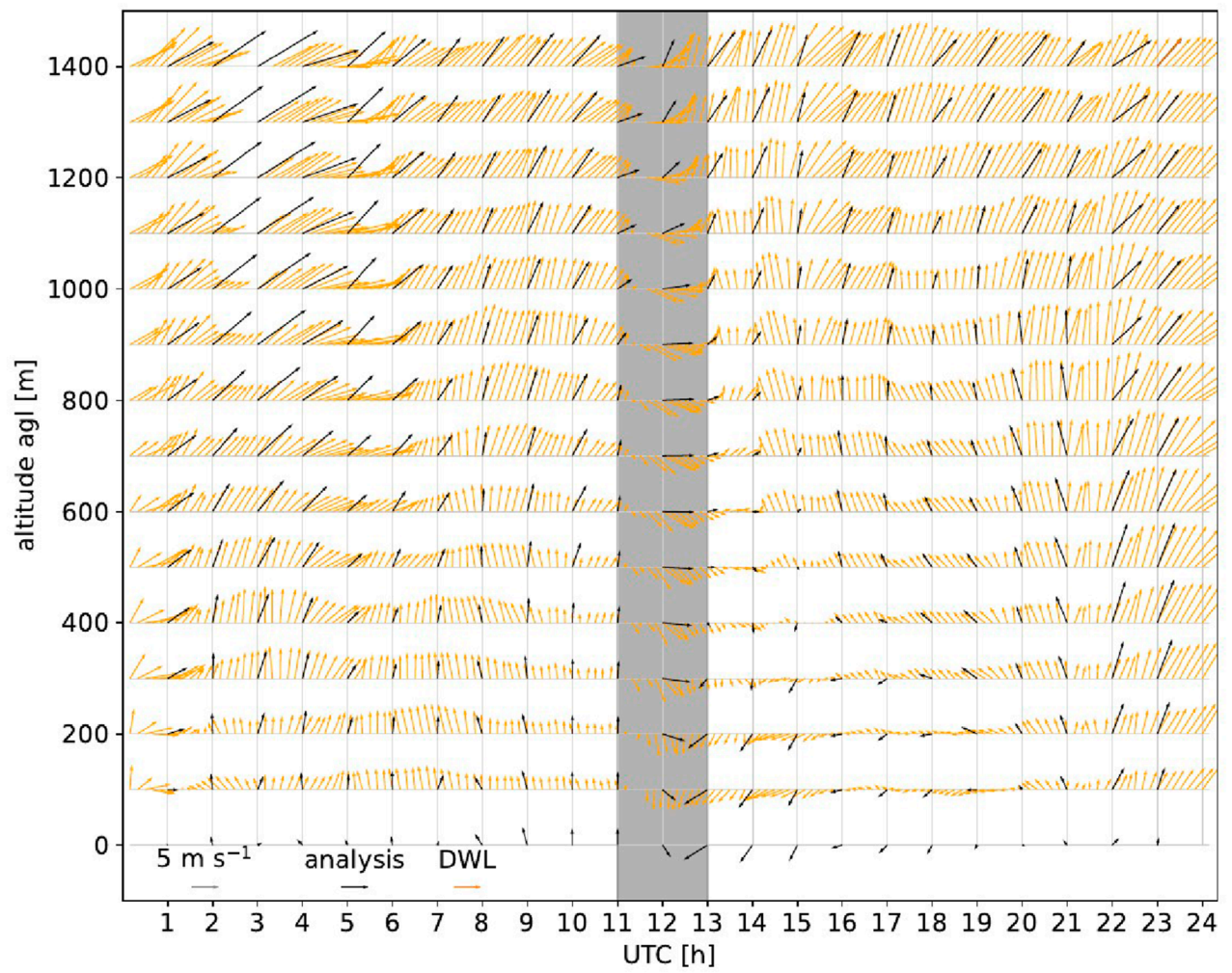

FIGURE 13
Evolution of vertical profiles of wind direction and speed above ground level (arrows) on 14 August at KITcube main site in Villingen-Schwenningen. Shown are 10 min Doppler wind lidar observations (DWL; orange) and 1 h ICON-D2 analysis fields (black). The precipitating period from 11 to 13 UTC is highlighted in grey.

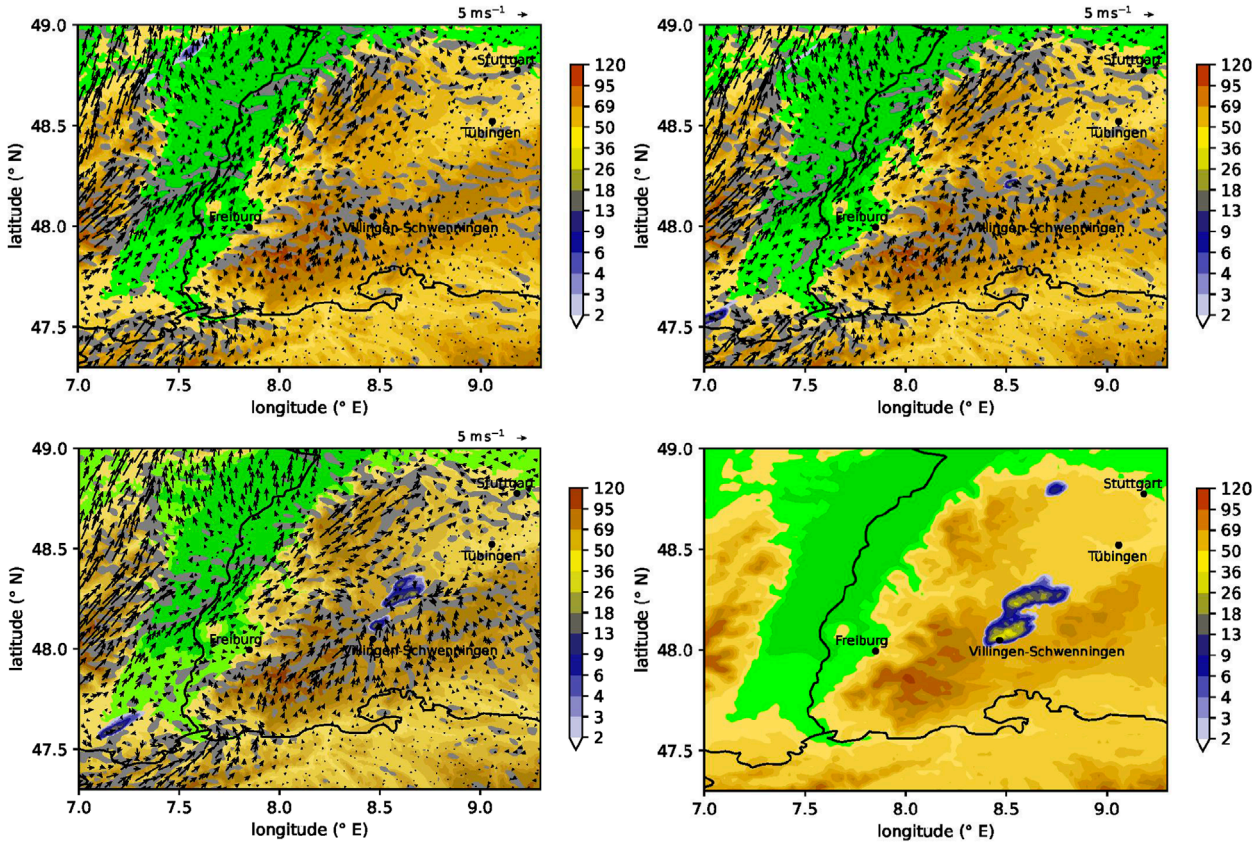

FIGURE 14
Simulated 500-m agl wind field (arrows) and wind convergence larger than $3.5{\cdot}10^{-4}$ s^{-1} (turquoise shades) with 30-min precipitation rate (in mm (30 min)$^{-1}$, colors) between 12:30 UTC and 13:30 UTC (top left and right, bottom left) and radar-derived hourly precipitation accumulations in mm h^{-1} (bottom right).

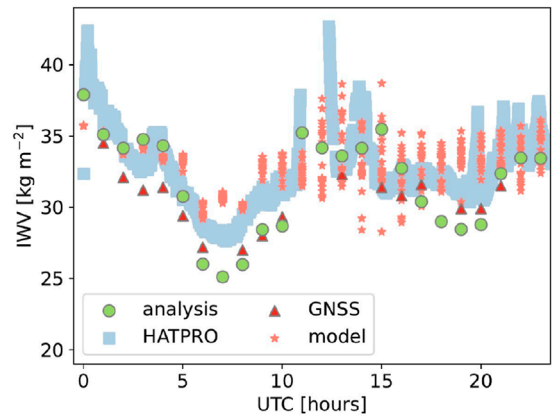

FIGURE 15
Evolution of IWV (kg m^{-2}) on 14 August 2023 at KITcube main site. Shown are IWV retrieved from microwave radiometer (HATPRO; square), GNSS (triangle), and ICON-D2 analysis (circle) data as well as from a microphysical model ensemble (model, asterisk) with differing horizontal resolution and CCN activation (Section 4.1) Microwave radiometer measurements were removed when the rain flag was raised.

content values simulated on the valley floor. Note that we show the results for 12:00 UTC, as this is the closest available time step to the ICON output at 11:00 UTC.

In short, this comparison showed that the hydrological models mHm and ParFlow generally capture the soil moisture distribution with more spatial heterogeneity and a more realistic water content than ICON analyses and forecasts, which use the less complex land surface model TERRA (Heise et al., 2006). Moreover, the ICON initial data make use of a soil moisture analysis, which tunes soil moisture and the Bowen ratio for better predictions of the 2-m temperature, which could help to explain the overall smaller agreement between ICON and the Rover measurements. The comparison also indicates the added value that high-resolution integrated hydrological models such as mHm and ParFlow may provide. Small-scale subsurface heterogeneity and hill slopes can be resolved, and sub-surface and surface hydrodynamics are linked. As shown in (Barlage et al., 2021), this also has a strong effect on L-A coupling, land water balance, and hydrometeorology in models such as ICON. Also, land-atmosphere feedbacks are scale-dependent and become more relevant at km-scale resolution with higher topographic gradients.

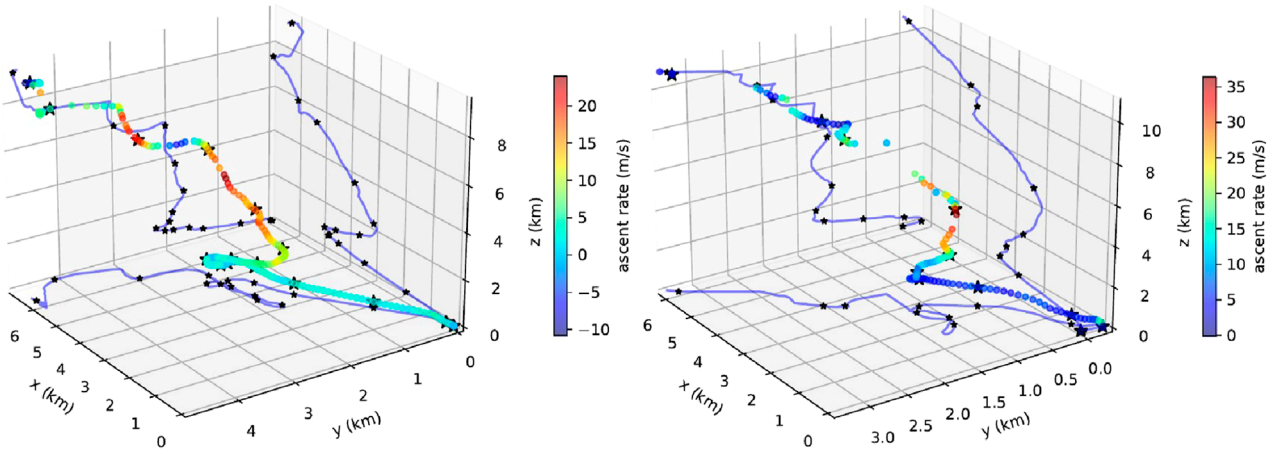

FIGURE 16
Trajectories of swarmsondes with vertical velocity (color bar in m s^{-1}) of two sondes launched at 11:57 (left) and 11:59 (right) on 14 August at 48.30079° N and 8.94849° E.

5.3 14 August 2023

One of the main reasons for conducting the Swabian MOSES field campaign was to assess whether lee-side convergence can help to explain the initiation of deep convection east of the Black Forest mountains. On 14 August 2023, convective cells developed east of the southern Black Forest mountain ridge, as indicated by RADOLAN observations (Figures 11, 12). More to the North, between Karlsruhe and Stuttgart, convection also developed east of the Northern Black Forest.

Around noon on 14 August, the ICON-D2 analysis shows a flow splitting around the Black Forest. At the southern tip of the Black Forest, the low-level flow diverges and splits into a northern branch directed towards the Rhine valley and a westerly branch that subsequently turns towards the north. In the lee of the Black Forest, a confluence zone is present and the flow converges (Figure 12). The convergence zone coincides with the convective cell. The network of Doppler wind lidar observations agrees mostly well with the ICON-D2 analysis. At the KITcube main site in Villingen-Schwenningen, the evolution of the wind direction and wind speed observations generally agree well with the ICON-D2 analysis (Figure 13). For example, the observations and ICON-D2 analysis show the southerly/southwesterly wind direction and increasing wind speed with height. However, local differences exist between the observations and the ICON-D2 analysis. In particular, during the passage of the convective cell in Villingen-Schwenningen the ICON-D2 analysis fails to capture the rapid change in wind direction. At 500 m agl, the onset of northerly/north-westerly flow is not captured; instead, the flow changes to westerly flow (Figure 13). After the passage of the convective cell, the southerly flow is recovered in both the observations and the ICON-D2 analysis. Despite differences in the representation of the local wind pattern in the ICON-D2 analysis, the lee-side convergence line associated with the convective cell is represented in the ICON-D2 analysis. The latter may result from the assimilation of operational (radar) observations in the operational analysis-forecasting cycle. In summary, the ICON-D2 analysis can capture the dominant flow characteristics, however, local differences to the observations exist and are particularly pronounced during convective events. This poses a challenge for the detailed process understanding of drivers of convection using analysis data. In the future, we will evaluate if the additional assimilation of the network of Doppler wind lidar observations improves the representation of the mesoscale circulation.

For that case, the ICON model with operationally used 2 km grid spacing does not produce deep convection at the observed locations (not shown). Although the model reproduces the south-westerly flow impinging on the Black Forest mountains, the convergence strength does not seem to be high enough to lift parcels to their respective level of free convection. A better result can be simulated when running the model at a finer resolution of 1 km (Figure 14) the southwesterly flow is deviated at the southern edge of the Southern Black Forest to the west and turns southwestward in the Rhine valley. The flow then turns to westerly directions in the Kinzig valley (separating the Northern and Southern Black Forest), and convergence occurs to the North of Villingen-Schwenningen when the flow meets the air from the south on the mountain's eastern side. As a result of low-level wind convergence, the first precipitation is simulated at 13:30 UTC. The simulated precipitation pattern is very similar to the radar-derived observations. This agreement demonstrates that a numerical model could reproduce the proposed mechanism for deep convection initiation by lee-side convergence. Still, a sufficiently high model resolution is necessary to produce enough updraft strength for convection initiation. The weaker convergence strength at 2 km grid spacing was already documented (e.g., Barthlott et al., 2024) and points towards the benefits of a finer grid resolution for simulating convection initiation in that area.

Similarly to 7 July, the different estimates of IWV agree concerning their diurnal evolution on 14 August (Figure 15). Initially, IWV decreases continuously until 07:00 UTC, and shows a substantial increase at the onset of precipitation. As discussed above (Figure 7), the microwave radiometers tend to overestimate IWV compared to GNSS retrievals and compared to the ICON-D2 analysis. The microphysical ensemble can capture the

temporal evolution of IWV approximately and exhibits the largest spread around noon during the precipitation event. No radiosondes were launched at Villingen-Schwenningen during that day.

Shortly before 12:00 UTC, the storm-chasing team positioned on the northeastern flank of a convective cell that showed some features of a weak supercell (cell south of Rottenburg in Figure 11). Two sondes were launched at 48.30079° N and 8.94849° E at time intervals of 3 min before heavy rain, wind gusts, and small hail prevented further balloon launches. During the first few minutes, both sondes drifted northeast with the cold pool at a low ascent speed around 2–3 m s^{-1} (Figure 16). About 15 min later and at an altitude of 1910 m above ground, the first launched sonde entered the cell's updraft, reaching an ascent speed of 24.0 m s^{-1}. The second sonde followed a similar trajectory but entered the updraft at about 4.4 km above ground, where a much higher updraft speed of 36.9 m s^{-1} was measured. The two balloons were already detached from the sonde at maximum ascent in both cases. An interesting feature is the spiral trajectory with a sequence of cyclonically/anticyclonically curved paths before entering the updraft, which was also observed on other days. The reasons for this are unclear and need further investigation.

6 Conclusions and outlook

In this paper, we presented the concept behind the "Swabian MOSES 2023″ measurement campaign that took place in the southern Black Forest, the Neckar Valley, and the Swabian Jura during the summer of 2023. The study area is known as a local hotspot for hail events. Based on the experience of the predecessor campaign, Swabian MOSES 2021, we shifted the meteorological observations southwestward to the region of Mount Feldberg ("trigger area"), while observations with a hydrological focus were concentrated in the Lindach catchment ("impact area"). In addition to the many instruments that measured continuously, radiosonde ascents were carried out on a total of 25 days in 8 IOPs, targeted CRNS rover runs were carried out, and a Storm Chasing Team was active on particularly convection-prone days. As in 2021, most of the instruments continued operating well into September, and thus beyond the end of the main measurement campaign. Although no further radiosonde ascents and no equipment maintenance or repairs were carried out, valuable observations were still recorded, especially in August.

The most significant events of the field campaign included IOP 2, which featured long-lived supercell storms in Northern Germany, while only weaker convective activity occurred in the Swabian MOSES domain. Within the observational area, IOP 5 stood out as the most impactful event, marked by strong convective cells and observed hail events, especially during the afternoon of 11 July. Additionally, several August cases had considerable impact, notably a hailstorm in the city of Reutlingen on 4 August, observed hail near Albstadt on 14 August, and a supercell storm on 24 August. In all of these events, however, no significant flooding events were reported.

Creating strong links between measurements and modeling was part of the campaign concept. This includes the validation of model results through field measurements and their assimilation into NWP models to fill gaps between measurements and investigate the impact on forecasts. Near real-time assimilation did not work out as envisaged due to technical reasons, but the data flow was successfully established, which will facilitate similar activities in future measurement campaigns. The foreseen assimilation experiments are currently being conducted in cooperation with DWD and will be examined as soon as possible. The validation of meteorological and hydrological models showed overall satisfactory agreement, for example, for the wind field. Differences between model and measurement are often no greater than those between different measurements, such as Doppler wind lidar and radiosonde. As expected, this applied least to the area immediately around convective events, although DWD already assimilates operational radar measurements. We found benefits in using the model at a finer resolution than the operational one, as well as in including aerosol effects with the use of a more sophisticated double-moment microphysical scheme. In some cases, however, simulations with coarser resolution fit the observations better. The comparison between modeled and measured soil moisture showed the superiority of the dedicated hydrological models over the operational TERRA soil model in ICON (Heise et al., 2006). We will continue to investigate the impact of soil moisture, including its representation in models, on convective initiation and intensification.

Important extensions of Swabian MOSES 2023 relative to 2021 (Kunz et al., 2022) are the larger investigation area, the better integration of modeling (i.e., hindcasts were run almost immediately after the events and assimilation of observational data), the involvement of citizen observers (e.g., hailstone collection), and the addition of new observation systems (DIAL and Raman lidar). Despite the overall successful and very comprehensive campaign, some devices, such as differential absorption lidars or Raman lidars, could only be applied on a testing level. In summary, Swabian MOSES 2023 has yielded a treasure trove of data that we will analyze in detail in the coming years. The two example events presented in this study already indicate the potential benefits of combining various observational systems and modeling strategies. The methodological developments and the interdisciplinary network between hydrology and meteorology established as part of the MOSES initiative provide a solid basis for further joint activities. For example, we hope that the assimilation of field data into operational prediction systems can be further explored during the TEAMx measurement campaign in the summer of 2025 (Serafin et al., 2020).

Data availability statement

The raw data supporting the conclusions of this article will be made available by the authors, without undue reservation.

Author contributions

JH: Conceptualization, Data curation, Investigation, Methodology, Software, Supervision, Writing – original draft,

Writing – review and editing. CB: Conceptualization, Data curation, Investigation, Methodology, Software, Supervision, Visualization, Writing – original draft, Writing – review and editing. MB: Conceptualization, Data curation, Investigation, Methodology, Software, Supervision, Visualization, Writing – original draft, Writing – review and editing. ABe: Data curation, Investigation, Methodology, Validation, Writing – original draft, Writing – review and editing. ABö: Investigation, Validation, Writing – original draft, Writing – review and editing. EB: Data curation, Investigation, Validation, Writing – original draft, Writing – review and editing. GD: Data curation, Investigation, Software, Validation, Writing – original draft, Writing – review and editing. PD: Conceptualization, Data curation, Investigation, Methodology, Project administration, Software, Supervision, Validation, Writing – original draft, Writing – review and editing. BF: Data curation, Investigation, Software, Validation, Writing – original draft, Writing – review and editing. GG: Data curation, Investigation, Validation, Writing – original draft, Writing – review and editing. KG: Data curation, Investigation, Software, Validation, Writing – original draft, Writing – review and editing. AG: Conceptualization, Data curation, Investigation, Software, Supervision, Validation, Writing – original draft, Writing – review and editing. SH: Data curation, Investigation, Software, Validation, Writing – original draft, Writing – review and editing. MH: Data curation, Formal Analysis, Validation, Writing – original draft. EH: Data curation, Investigation, Software, Visualization, Writing – original draft, Writing – review and editing. MilK: Data curation, Investigation, Validation, Writing – original draft, Writing – review and editing. JK: Data curation, Investigation, Methodology, Software, Supervision, Validation, Writing – original draft, Writing – review and editing. MarK: Conceptualization, Data curation, Investigation, Methodology, Software, Validation, Writing – original draft, Writing – review and editing. PK: Conceptualization, Funding acquisition, Investigation, Methodology, Project administration, Software, Supervision, Validation, Writing – original draft, Writing – review and editing. MicK: Data curation, Investigation, Methodology, Software, Supervision, Validation, Writing – original draft, Writing – review and editing. SL: Data curation, Investigation, Software, Validation, Writing – original draft, Writing – review and editing. YL: Data curation, Investigation, Software, Validation, Writing – original draft, Writing – review and editing. MeM: Data curation, Investigation, Validation, Writing – original draft, Writing – review and editing. OM: Conceptualization, Data curation, Investigation, Methodology, Software, Supervision, Validation, Writing – original draft, Writing – review and editing. MoM: Data curation, Investigation, Validation, Writing – original draft, Writing – review and editing. HN: Data curation, Investigation, Software, Validation, Writing – original draft, Writing – review and editing. NN: Data curation, Investigation, Software, Validation, Writing – original draft, Writing – review and editing. AO: Conceptualization, Data curation, Formal Analysis, Investigation, Methodology, Software, Supervision, Validation, Visualization, Writing – original draft, Writing – review and editing. OR: Data curation, Investigation, Validation, Writing – original draft, Writing – review and editing. HR: Data curation, Investigation, Validation, Writing – original draft, Writing – review and editing. MR: Conceptualization, Data curation, Investigation, Methodology, Software, Validation, Writing – original draft, Writing – review and editing. HS: Conceptualization, Data curation, Investigation, Methodology, Software, Supervision, Validation, Visualization, Writing – original draft, Writing – review and editing. LS: Conceptualization, Data curation, Investigation, Methodology, Software, Validation, Writing – original draft, Writing – review and editing. MS: Data curation, Investigation, Methodology, Software, Validation, Writing – original draft, Writing – review and editing. CS: Writing – original draft, Writing – review and editing. TS: Writing – original draft, Writing – review and editing. FV: Data curation, Investigation, Validation, Writing – original draft, Writing – review and editing. SV: Data curation, Investigation, Validation, Writing – original draft, Writing – review and editing. UW: Writing – original draft, Writing – review and editing. AW: Conceptualization, Data curation, Investigation, Methodology, Project administration, Software, Supervision, Validation, Writing – original draft, Writing – review and editing. HZ: Data curation, Investigation, Validation, Writing – original draft, Writing – review and editing.

Funding

The author(s) declare that financial support was received for the research and/or publication of this article. This work was supported by funding from the Helmholtz Association within the framework of MOSES. AO is supported by the Italia—Deutschland science-4-services network in weather and climate (IDEA-S4S, project INVACODA, funding no. 4823IDEAP6). This Italian-German research network of universities, research institutes, and Deutscher Wetterdienst is funded by the BMDV (Federal Ministry of Digital and Transport). YL acknowledges funding by the China Scholarship Council (CSC). HN and NDN are funded by the Helmholtz Climate Initiative (HICAM). ABe, KG, and SH were funded by the BMBF BioökonomieREVIER funding scheme with its BioRevierPlus project (funding reference 031B1137D/031B1137DX).

Acknowledgments

The execution of the measurement campaign would not have been possible without the tireless efforts of the technical staff and student workers, even on weekends and at night. The authors wish to thank the German Weather Service (DWD) for providing the ICON model code, the initial and boundary data as well as RADOLAN data, and logistic support on Mt. Feldberg. The authors gratefully acknowledge the computing time provided on the high-performance computer HoreKa by the National High-Performance Computing Center at KIT (NHR@KIT). This center is jointly supported by the Federal Ministry of Education and Research and the Ministry of Science, Research and the Arts of Baden-Württemberg, as part of the National High-Performance Computing (NHR) joint funding program (https://www.nhr-verein.de/en/our-partners). HoreKa is partly funded by the German Research Foundation (DFG). The Large Scale Data Facility is founded and supported by the Helmholtz research programme "Supercomputing" of the Helmholtz Association of German Research Centres and of the Ministry for Science, Research

and Arts (MWK) of the state of Baden-Württemberg. We also gratefully acknowledge the Gauss Centre for Supercomputing e.V. (www.gauss-centre.eu) for providing computing time through the John von Neumann Institute for Computing (NIC) on the GCS Supercomputer JUWELS at Jülich Supercomputing Centre (JSC).

Conflict of interest

The authors declare that the research was conducted in the absence of any commercial or financial relationships that could be construed as a potential conflict of interest.

Generative AI statement

The author(s) declare that Generative AI was used in the creation of this manuscript. "Grammarly" generative AI (https://app.grammarly.com/) was used for the whole article's grammar, spelling, and stylistic check.

Publisher's note

All claims expressed in this article are solely those of the authors and do not necessarily represent those of their affiliated organizations, or those of the publisher, the editors and the reviewers. Any product that may be evaluated in this article, or claim that may be made by its manufacturer, is not guaranteed or endorsed by the publisher.

Supplementary Material

The Supplemnentary Material for this article can be found online at: https://www.frontiersin.org/articles/10.3389/feart.2025.1555755/full#supplementary-material

References

Apel, H., Vorogushyn, S., and Merz, B. (2022). Brief communication: impact forecasting could substantially improve the emergency management of deadly floods: case study july 2021 floods in Germany. *Nat. Hazards Earth Syst. Sci.* 22, 3005–3014. doi:10.5194/nhess-22-3005-2022

Barlage, M., Chen, F., Rasmussen, R., Zhang, Z., and Miguez-Macho, G. (2021). The importance of scale-dependent groundwater processes in land-atmosphere interactions over the central United States. *Geophys. Res. Lett.* 48. doi:10.1029/2020GL092171

Bartels, H. (2004). Projekt RADOLAN - Routineverfahren zur Online-Aneichung der Radarniederschlagsdaten mit Hilfe von automatischen Bodenniederschlagsstationen (Ombrometer). Available online at: https://www.dwd.de/DE/leistungen/radolan/radolan.html (Accessed November 4, 2024).111

Barthlott, C., Czajka, B., Kunz, M., Saathoff, H., Zhang, H., Böhmländer, A., et al. (2024). The impact of aerosols and model grid spacing on a supercell storm from Swabian MOSES 2021. *Quart. J. Roy. Meteor. Soc.* 150, 2005–2027. doi:10.1002/qj.4687

Barthlott, C., and Hoose, C. (2015). Spatial and temporal variability of clouds and precipitation over Germany: multiscale simulations across the "gray zone". *Atmos. Chem. Phys.* 15, 12361–12384. doi:10.5194/acp-15-12361-2015

Barthlott, C., Mühr, B., and Hoose, C. (2017). Sensitivity of the 2014 Pentecost storms over Germany to different model grids and microphysics schemes. *Quart. J. Roy. Meteor. Soc.* 143, 1485–1503. doi:10.1002/qj.3019

Barthlott, C., Zarboo, A., Matsunobu, T., and Keil, C. (2022). Impacts of combined microphysical and land-surface uncertainties on convective clouds and precipitation in different weather regimes. *Atmos. Chem. Phys.* 22, 10841–10860. doi:10.5194/acp-22-10841-2022

Bates, P. D., Horritt, M. S., and Fewtrell, T. J. (2010). A simple inertial formulation of the shallow water equations for efficient two-dimensional flood inundation modelling. *J. Hydrology* 387, 33–45. doi:10.1016/j.jhydrol.2010.03.027

Bechtold, P., Köhler, M., Jung, T., Doblas-Reyes, F., Leutbecher, M., Rodwell, M. J., et al. (2008). Advances in simulating atmospheric variability with the ECMWF model: from synoptic to decadal time-scales. *Quart. J. Roy. Meteor. Soc.* 134, 1337–1351. doi:10.1002/qj.289

Belleflamme, A., Goergen, K., Wagner, N., Kollet, S., Bathiany, S., El Zohbi, J., et al. (2023). Hydrological forecasting at impact scale: the integrated parflow hydrological model at 0.6 km for climate resilient water resource management over Germany. *Front. Water* 5. doi:10.3389/frwa.2023.1183642

Bishop, C. H., Etherton, B. J., and Majumdar, S. J. (2001). Adaptive sampling with the ensemble transform kalman filter. Part I: theoretical aspects. *Mon. Weather Rev.* 129, 420–436. doi:10.1175/1520-0493(2001)129<0420:aswtet>2.0.co;2

Blahak, U. (2025). Development of DWD´s seamless integrated forecasting system. Available online at: https://www.dwd.de/EN/research/researchprogramme/sinfony_iafe/sinfony_en_node.html (Accessed May 13, 2025).

Boeing, F., Rakovec, O., Kumar, R., Samaniego, L., Schrön, M., Hildebrandt, A., et al. (2022). High-resolution drought simulations and comparison to soil moisture observations in Germany. *Hydrology Earth Syst. Sci.* 26, 5137–5161. doi:10.5194/hess-26-5137-2022

Boeing, F., Wagener, T., Marx, A., Rakovec, O., Kumar, R., Samaniego, L., et al. (2024). Increasing influence of evapotranspiration on prolonged water storage recovery in Germany. *Environ. Res. Lett.* 19, 024047. doi:10.1088/1748-9326/ad24ce

Brookfield, A. E., Ajami, H., Carroll, R. W. H., Tague, C., Sullivan, P. L., and Condon, L. E. (2023). Recent advances in integrated hydrologic models: integration of new domains. *J. Hydrology* 620, 129515. doi:10.1016/j.jhydrol.2023.129515

[Dataset] BGR (2014). Digital soil map of Germany 1:200,000 (BUEK200) v0.5. Available online at: https://www.bgr.bund.de/DE/Themen/Boden/Informationsgrundlagen/Bodenkundliche_Karten_Datenbanken/BUEK200/buek200_node.h (Accessed on October 7, 2022).

Desilets, D., Zreda, M., and Ferré, T. P. (2010). Nature's neutron probe: land surface hydrology at an elusive scale with cosmic rays. *Water Resour. Res.* 46. doi:10.1029/2009wr008726

Dirmeyer, P. A., Schlosser, C. A., and Brubaker, K. L. (2009). Precipitation, recycling, and land memory: an integrated analysis. *J. Hydrometeorol.* 10, 278–288. doi:10.1175/2008JHM1016.1

Fatima, E., Kumar, R., Attinger, S., Kaluza, M., Rakovec, O., Rebmann, C., et al. (2023). Improved representation of soil moisture simulations through incorporation of cosmic-ray neutron count measurements in a large-scale hydrologic model. *EGUsphere* 2023, 1–33. doi:10.5194/egusphere-2023-1548

Gupta, H. V., and Kling, H. (2011). On typical range, sensitivity, and normalization of Mean Squared Error and Nash-Sutcliffe Efficiency type metrics. *Water Resour. Res.* 47. doi:10.1029/2011wr010962

Hande, L. B., Engler, C., Hoose, C., and Tegen, I. (2015). Seasonal variability of Saharan desert dust and ice nucleating particles over Europe. *Atmos. Chem. Phys.* 15, 4389–4397. doi:10.5194/acp-15-4389-2015

Hargreaves, G. H., and Samani, Z. A. (1985). Reference crop evapotranspiration from temperature. *Appl. Eng. Agric.* 1, 96–99. doi:10.13031/2013.26773

Heise, E., Ritter, B., and Schrodin, E. (2006). Operational implementation of the multilayer soil model TERRA. *Tech. Rep.* 9, 19. doi:10.5676/DWD_pub/nwv/cosmo-tr_9

Hogan, R. J., and Bozzo, A. (2018). A flexible and efficient radiation scheme for the ECMWF model. *J. Adv. Model. Earth Syst.* 10, 1990–2008. doi:10.1029/2018MS001364

Hunt, B. R., Kostelich, E. J., and Szunyogh, I. (2007). Efficient data assimilation for spatiotemporal chaos: a local ensemble transform Kalman filter. *Phys. D. Nonlinear Phenom.* 230, 112–126. doi:10.1016/j.physd.2006.11.008

Kalthoff, N., Adler, B., Wieser, A., Kohler, M., Träumner, K., Handwerker, J., et al. (2013). KITcube–a mobile observation platform for convection studies deployed during HyMeX. *Meteor. Z.* 22, 633–647. doi:10.1127/0941-2948/2013/0542

Kärcher, B., Hendricks, J., and Lohmann, U. (2006). Physically based parameterization of cirrus cloud formation for use in global atmospheric models. *J. Geophys. Res.* 111. doi:10.1029/2005jd006219

Kärcher, B., and Lohmann, U. (2002). A parameterization of cirrus cloud formation: homogeneous freezing of supercooled aerosols. *J. Geophys. Res.* 107, 4–10. doi:10.1029/2001JD000470

Köhli, M., Schrön, M., Zreda, M., Schmidt, U., Dietrich, P., and Zacharias, S. (2015). Footprint characteristics revised for field-scale soil moisture monitoring with cosmic-ray neutrons. *Water Resour. Res.* 51, 5772–5790. doi:10.1002/2015WR017169

Koster, R. D., Dirmeyer, P. A., Guo, Z., Bonan, G., Chan, E., Cox, P., et al. (2004). Regions of strong coupling between soil moisture and precipitation. *Science* 305, 1138–1140. doi:10.1126/science.1100217

Kuffour, B. N. O., Engdahl, N. B., Woodward, C. S., Condon, L. E., Kollet, S., and Maxwell, R. M. (2020). Simulating coupled surface–subsurface flows with parflow v3.5.0: capabilities, applications, and ongoing development of an open-source, massively parallel, integrated hydrologic model. *Geosci. Model Dev.* 13, 1373–1397. doi:10.5194/gmd-13-1373-2020

Kumar, R., Samaniego, L., and Attinger, S. (2013). Implications of distributed hydrologic model parameterization on water fluxes at multiple scales and locations. *Water Resour. Res.* 49, 360–379. doi:10.1029/2012wr012195

Kunz, M., Abbas, S. S., Bauckholt, M., Böhmländer, A., Feuerle, T., Gasch, P., et al. (2022). Swabian moses 2021: an interdisciplinary field campaign for investigating convective storms and their event chains. *Front. Earth Sci.* 10. doi:10.3389/feart.2022.999593

Leuenberger, D., Koller, M., Fuhrer, O., and Schär, C. (2010). A generalization of the SLEVE vertical coordinate. *Mon. Wea. Rev.* 138, 3683–3689. doi:10.1175/2010MWR3307.1

Markowski, P. M., Richardson, Y. P., Richardson, S. J., and Petersson, A. (2018). Aboveground thermodynamic observations in convective storms from balloonborne probes acting as pseudo-Lagrangian drifters. *Bull. Amer. Meteor. Soc.* 99, 711–724. doi:10.1175/BAMS-D-17-0204.1

Mauder, M., Cuntz, M., Drüe, C., Graf, A., Rebmann, C., Schmid, H. P., et al. (2013). A strategy for quality and uncertainty assessment of long-term eddy-covariance measurements. *Agric. For. Meteorology* 169, 122–135. doi:10.1016/j.agrformet.2012.09.006

Merz, B., Kuhlicke, C., Kunz, M., Pittore, M., Babeyko, A., Bresch, D. N., et al. (2020a). Impact forecasting to support emergency management of natural hazards. *Rev. Geophys.* 58. doi:10.1029/2020RG000704

Merz, R., Tarasova, L., and Basso, S. (2020b). The flood cooking book: ingredients and regional flavors of floods across Germany. *Environ. Res. Lett.* 15, 114024. doi:10.1088/1748-9326/abb9dd

Möhler, O., Adams, M., Lacher, L., Vogel, F., Nadolny, J., Ullrich, R., et al. (2021). The Portable Ice Nucleation Experiment (PINE): a new online instrument for laboratory studies and automated long-term field observations of ice-nucleating particles. *Atmos. Meas. Tech.* 14, 1143–1166. doi:10.5194/amt-14-1143-2021

Najafi, H., Shrestha, P. K., Rakovec, O., Apel, H., Vorogushyn, S., Kumar, R., et al. (2024). High-resolution impact-based early warning system for riverine flooding. *Nat. Commun.* 15, 3726. doi:10.1038/s41467-024-48065-y

Nesbitt, S. W., Salio, P. V., Ávila, E., Bitzer, P., Carey, L., Chandrasekar, V., et al. (2021). A storm safari in subtropical south America: proyecto relampago. *Bull. Am. Meteorological Soc.* 102, E1621–E1644. doi:10.1175/BAMS-D-20-0029.1

Puskeiler, M., Kunz, M., and Schmidberger, M. (2016). Hail statistics for Germany derived from single-polarization radar data. *Atmos. Res.* 178-179, 459–470. doi:10.1016/j.atmosres.2016.04.014

Rakovec, O., Kumar, R., Attinger, S., and Samaniego, L. (2016a). Improving the realism of hydrologic model functioning through multivariate parameter estimation. *Water Resour. Res.* 52, 7779–7792. doi:10.1002/2016wr019430

Rakovec, O., Kumar, R., Mai, J., Cuntz, M., Thober, S., Zink, M., et al. (2016b). Multiscale and multivariate evaluation of water fluxes and states over European river basins. *J. Hydrometeorol.* 17, 287–307. doi:10.1175/jhm-d-15-0054.1

Raschendorfer, M. (2001). The new turbulence parameterization of LM. *COSMO Newsl.* 1, 89–97. Available online at: https://www.cosmo-model.org/content/model/documentation/newsLetters/newsLetter01/newsLetter_01.pdf

Rauthe, M., Steiner, H., Riediger, U., Mazurkiewicz, A., and Gratzki, A. (2013). A central european precipitation climatology–part i: generation and validation of a high-resolution gridded daily data set (hyras). *Meteorol. Z.* 22, 235–256. doi:10.1127/0941-2948/2013/0436

Reinert, D., Prill, F., Frank, H., Denhard, M., Baldauf, M., Schraff, C., et al. (2024). "DWD database reference for the global and regional ICON and ICON-eps forecasting system version 2.3.1," in *Icon database reference manual*. German Weather Service. Available online at: https://www.dwd.de/DE/leistungen/nwv_icon_modelldokumentation/nwv_icon_modelldokumentation.html?nn=495490.

Richter, R. (1996). A spatially adaptive fast atmospheric correction algorithm. *Int. J. Remote Sens.* 17, 1201–1214. doi:10.1080/01431169608949077

Richter, R. (2003). Report of Institute IMF, DLR-IB 564-03/03: *value adding products derived from the ATCOR models (version 5.5, January 2003).* Available online at: https://www.rese.ch/pdf/atcor_value_adding.pdf.

Rieger, D., Bangert, M., Bischoff-Gauss, I., Förstner, J., Lundgren, K., Reinert, D., et al. (2015). Icon–art 1.0 – a new online-coupled model system from the global to regional scale. *Geosci. Model Dev.* 8, 1659–1676. doi:10.5194/gmd-8-1659-2015

Rotach, M. W., Serafin, S., Ward, H. C., Arpagaus, M., Colfescu, I., Cuxart, J., et al. (2022). A collaborative effort to better understand, measure, and model atmospheric exchange processes over mountains. *Bull. Am. Meteorological Soc.* 103, E1282–E1295. doi:10.1175/BAMS-D-21-0232.1

Saadi, M., Furusho-Percot, C., Belleflamme, A., Chen, J. Y., Trömel, S., and Kollet, S. (2023). How uncertain are precipitation and peak flow estimates for the july 2021 flooding event? *Nat. Hazards Earth Syst. Sci.* 23, 159–177. doi:10.5194/nhess-23-159-2023

Samaniego, L., Kumar, R., and Attinger, S. (2010). Multiscale parameter regionalization of a grid-based hydrologic model at the mesoscale. *Water Resour. Res.* 46. doi:10.1029/2008wr007327

Samaniego, L., Kumar, R., and Jackisch, C. (2011). Predictions in a data-sparse region using a regionalized grid-based hydrologic model driven by remotely sensed data. *Hydrology Res.* 42, 338–355. doi:10.2166/nh.2011.156

Schneider, J., Höhler, K., Heikkilä, P., Keskinen, J., Bertozzi, B., Bogert, P., et al. (2021). The seasonal cycle of ice-nucleating particles linked to the abundance of biogenic aerosol in boreal forests. *Atmos. Chem. Phys.* 21, 3899–3918. doi:10.5194/acp-21-3899-2021

Schneider, L., Barthlott, C., Hoose, C., and Barrett, A. I. (2019). Relative impact of aerosol, soil moisture, and orography perturbations on deep convection. *Atmos. Chem. Phys.* 19, 12343–12359. doi:10.5194/acp-19-12343-2019

Schraff, C., Reich, H., Rhodin, A., Schomburg, A., Stephan, K., Periáñez, A., et al. (2016). Kilometre-scale ensemble data assimilation for the COSMO model (KENDA). *Q. J. R. Meteorological Soc.* 142, 1453–1472. doi:10.1002/qj.2748

Schrön, M., Rosolem, R., Köhli, M., Piussi, L., Schröter, I., Iwema, J., et al. (2018). Cosmic-ray neutron rover surveys of field soil moisture and the influence of roads. *Water Resour. Res.* 54, 6441–6459. doi:10.1029/2017WR021719

Segal, Y., and Khain, A. (2006). Dependence of droplet concentration on aerosol conditions in different cloud types: application to droplet concentration parameterization of aerosol conditions. *J. Geophys. Res.* 111. doi:10.1029/2005JD006561

Seifert, A., and Beheng, K. D. (2006). A two-moment cloud microphysics parameterization for mixed-phase clouds. Part 2: maritime vs. continental deep convective storms. *Meteorol. Atmos. Phys.* 92, 67–82. doi:10.1007/s00703-005-0113-3

Seifert, A., Köhler, C., and Beheng, K. (2012). Aerosol-cloud-precipitation effects over Germany as simulated by a convective-scale numerical weather prediction model. *Atmos. Chem. Phys.* 12, 709–725. doi:10.5194/acp-12-709-2012

Serafin, S., Rotach, M. W., Arpagaus, M., Colfescu, I., Cuxart, J., Wekker, S. F. J. D., et al. (2020). *Multi-scale transport and exchange processes in the atmosphere over mountains*. Innsbruck, Austria: Innsbruck University Press. doi:10.15203/99106-003-1

Tiedtke, M. (1989). A comprehensive mass flux scheme for cumulus parameterization in large-scale models. *Mon. Wea. Rev.* 117, 1779–1800. doi:10.1175/1520-0493(1989)117<1779:acmfsf>2.0.co;2

Varble, A. C., Nesbitt, S. W., Salio, P., Hardin, J. C., Bharadwaj, N., Borque, P., et al. (2021). Utilizing a storm-generating hotspot to study convective cloud transitions: the cacti experiment. *Bull. Am. Meteorological Soc.* 102, E1597–E1620. doi:10.1175/BAMS-D-20-0030.1

Weber, U., Attinger, S., Baschek, B., Boike, J., Borchardt, D., Brix, H., et al. (2022). MOSES: a novel observation system to monitor dynamic events across earth compartments. *Bull. Amer. Meteor. Soc.* 103, E339–E348. doi:10.1175/BAMS-D-20-0158.1

Wieser, A., Güntner, A., Dietrich, P., Handwerker, J., Khordakova, D., Ködel, U., et al. (2022). First implementation of a new cross-disciplinary observation strategy for heavy precipitation events from formation to flooding. *Hydrol. Earth Syst. Sci. Discuss. , rev*. doi:10.5194/hess-2022-131

Wilson, J., and Schreiber, W. (1986). Initiation of convective storms at radar-observed boundary-layer convergence lines. *Mon. Wea. Rev.* 114, 2516–2536. doi:10.1175/1520-0493(1986)114<2516:iocsar>2.0.co;2

Wloczyk, C. (2007). *Entwicklung und validierung einer methodik zur ermittlung der realen evapotranspiration anhand von fernerkundungsdaten in Mecklenburg-Vorpommern*. (PhD thesis). Universität Rostock.

Zängl, G., Reinert, D., Rípodas, P., and Baldauf, M. (2015). The ICON (ICOsahedral Non-hydrostatic) modelling framework of DWD and MPI-M: description of the non-hydrostatic dynamical core. *Quart. J. Roy. Meteor. Soc.* 141, 563–579. doi:10.1002/qj.2378

Zhang, H., Wagner, F., Saathoff, H., Vogel, H., Hoshyaripour, G., Bachmann, V., et al. (2022). Comparison of scanning LiDAR with other remote sensing measurements and Transport model predictions for a saharan dust case. *Remote Sens.* 14, 1693. doi:10.3390/rs14071693

Zink, M., Mai, J., Cuntz, M., and Samaniego, L. (2018). Conditioning a hydrologic model using patterns of remotely sensed land surface temperature. *Water Resour. Res.* 54, 2976–2998. doi:10.1002/2017wr021346

Zreda, M., Shuttleworth, W. J., Zeng, X., Zweck, C., Desilets, D., Franz, T., et al. (2012). COSMOS: the COsmic-ray soil moisture observing system. *Hydrology Earth Syst. Sci.* 16, 4079–4099. doi:10.5194/hess-16-4079-2012